Gas Phase Infrared Spectroscopy of Glycolipids

Master Thesis

accomplished in the Group of
Prof. Dr. Kevin Pagel and
Prof. Dr. Gert von Helden
at the Fritz Haber Institute
04.03.2019 – 22.08.2019

Carla Kirschbaum

Supervisor:	M.Sc. Eike Mucha
First Examiner:	Prof. Dr. Kevin Pagel
Second Examiner:	Prof. Dr. Christoph A. Schalley

Abstract

Carbohydrates and lipids are not only energy sources and structural components of cells but fulfill very diverse and important roles in a multitude of cellular processes. The combination of a carbohydrate and a lipid linked *via* a glycosidic bond yields a glycolipid. Glycolipids occur in all kinds of organisms where they constitute major components of cell membranes, mediate cell-cell interactions and modulate immune responses. Their biological activities are highly dependent on their exact three-dimensional structures; however, the elucidation of glycolipid structures is inherently challenging due to the non-template-driven regio- and stereoselective synthesis of the carbohydrate and additional variations of the lipid moiety, such as length, saturation and hydroxylation. The modular biosynthesis of glycolipids generates many different and often isomeric combinations of glycans and lipids, which are not always distinguishable by standard analytical workflows based on liquid chromatography-mass spectrometry. The structural analysis of isomeric glycolipids thus requires orthogonal techniques yielding complementary information. In some cases, ion mobility spectrometry can be used to distinguish isomers based on their different cross sections in the gas phase. Another promising structure-sensitive technique is cryogenic gas phase infrared spectroscopy, which falls under the term *action spectroscopy* and yields highly resolved, reproducible IR spectra of isolated ions in the clean gas phase environment.

In this work, sets of isomeric glycolipids were systematically investigated using ion mobility-mass spectrometry and cryogenic gas phase IR spectroscopy in helium nanodroplets. The obtained IR spectra of various isomeric glycosphingolipids bearing different monosaccharide headgroups are diagnostic for both the type of monosaccharide and the anomeric configuration because of very characteristic and reproducible absorption bands in the fingerprint region (1000–1150 cm^{-1}). A more complex trisaccharide headgroup still yields a well-resolved IR fingerprint. The influence of the lipid part was examined by comparing IR spectra of glycolipids bearing the same headgroup but a different sphingoid base or a diacylglycerol. The exchange of phytosphingosine for sphingosine does not alter the fingerprint region significantly but influences the intensity of the amine bending vibration, whereas the introduction of a diacylglycerol changes the whole spectrum. The data show that cryogenic gas phase IR spectroscopy is a powerful technique to distinguish glycolipids bearing isomeric glycans up to a certain size, anomeric configurations and also subtle variations in the lipid moiety. Furthermore, the applicability of IR spectroscopy to distinguish double bond isomers was tested on synthetic derivatives of 1-deoxysphingosine. Depending on the position and configuration of the C=C double bond, distinct N−H bending modes of the protonated amine are observed. Gas phase IR spectroscopy could thus fill a gap in lipidomics, where lipid double bond isomers still pose a major challenge.

Abbreviations

CCS	Collision cross section
CID	Collision-induced dissociation
CoA	Coenzyme A
DC	Direct current
DMS	Differential-mobility spectrometry
DT	Drift tube
ESI	Electrospray ionization
FEL	Free electron laser
Gal	Galactose
GalCer	Galactosylceramide
Gb3	Globotriaosylceramide
Glc	Glucose
GlcA	Glucuronic acid
GSL	Glycosphingolipid
HSAN1	Hereditary sensory and autonomic neuropathy type 1
IMS	Ion mobility spectrometry
IR	Infrared
IRMPD	Infrared multiple-photon dissociation
IVR	Intramolecular vibrational redistribution
LC	Liquid chromatography
MS	Mass spectrometry
NKT cells	Natural killer T cells
NMR	Nuclear magnetic resonance
OzID	Ozone-induced dissociation
TOF	Time-of-flight
UV	Ultraviolet

Contents

Abstract I

Abbreviations III

1. Introduction 1

1.1 Motivation 1

1.2 Aim of this Thesis 2

2. Fundamentals 3

2.1 Biological Relevance of Carbohydrates and Lipids 3

2.2 Glycolipids 4

2.3 Structural Analysis of Glycolipids 7

2.4 Ion Mobility-Mass Spectrometry 9

2.5 Gas Phase Infrared Spectroscopy 11

3. Experimental Section 15

3.1 Sample Preparation 15

3.2 Ion Mobility Measurements 18

3.3 Cryogenic Gas Phase Infrared Spectroscopy in Helium Droplets 19

3.4 Data Processing 21

4. Results and Discussion 23

4.1 Structural Diversity of the Glycan and Anomeric Configuration 23

4.1.1 Monoglycosyl Phytosphingosines 23

4.1.2 Globotriaosylceramide 30

4.2 Structural Diversity of the Lipid 32

4.2.1 Monoglycosyl Sphingosines 32

4.2.2 Glycoglycerolipids 38

4.2.3 1-Deoxysphingolipids 41

5. Conclusions and Outlook 49

References VII

Acknowledgments XI

Statutory Declaration XIII

1. Introduction

1.1 Motivation

Glycolipids, glycoconjugates formed by the covalent attachment of a carbohydrate to a lipid moiety, are required for multiple cellular processes ensuring the development and function of multicellular organisms.[1] Yet, glycolipids are still largely understudied due to the lack of accurate and sensitive analytical methods.[2] The need for new analytical tools allowing reliable structure determination – especially of naturally low abundant glycolipids – is illustrated by the following example from recent research, which constituted the starting point and the motivation for this thesis.

Natural killer T cells (NKT cells) are lymphocytes, which are triggered by endogenous ligands to ensure the fast initiation of immune responses.[3] The nature of the activating ligands remained unknown for more than a decade after the discovery of NKT cells.[4] Early biological assays revealed that α-glycosylceramides were stimulating NKT cells in vitro; however, α-glycosylceramides could not be detected in mammals.[5] The only two identified mammalian glycosylceramide synthases are inverting transferases producing exclusively β-glycosylceramides, and the sensitivity of standard chemical analytical techniques is too low to confirm the possible presence of α-isomers below 1 %.[6] Nevertheless, when isolated from animal sources, the supposed β-glycosylceramides activated NKT cells with a batch-dependent effectiveness.[4] β-Glycosylceramides could not be responsible for the activation because their lack of stimulatory activity was known and because β-glycosylceramides are too abundant in mammals to selectively trigger NKT cells in case of an infection and cease their activity afterwards.[3,6] The enigma was solved by Kain *et al.* in a study published in 2014. They proved by a combination of biological, immunological and enzymatic assays that α-glycosylceramides are produced by mammalian immune cells at a very low and tightly controlled level.[6] The search for endogenous ligands of NKT cells illustrates the discrepancy of sensitivity between biological and chemical analytical methods: biological assays proved the activity of a natural mixture of α- and β-glycosylceramides, but standard chemical analytical methods were not sensitive enough to detect the low abundant α-isomer solely responsible for the observed activation of NKT cells.

In this respect, sensitive analytical techniques to differentiate α- and β-isomers and preferably also allowing a more comprehensive characterization of glycolipids are urgently needed. In a research project in 2018, we investigated the isomeric α- and β-galactosylceramides (GalCer) described by Kain *et al.*[4] by complementary gas phase analytical techniques: ion mobility-mass spectrometry (IM-MS) and cryogenic gas phase infrared (IR) spectroscopy in helium droplets. IM-MS did not resolve the difference between the two isomers, but gas phase IR spectroscopy yielded diagnostic spectra of protonated and sodiated GalCer (Fig. 1). The diagnostic absorptions allowing an unambiguous distinction of α- and β-GalCer are located in a narrow spectral range from 950 cm^{-1} to 1150 cm^{-1}.

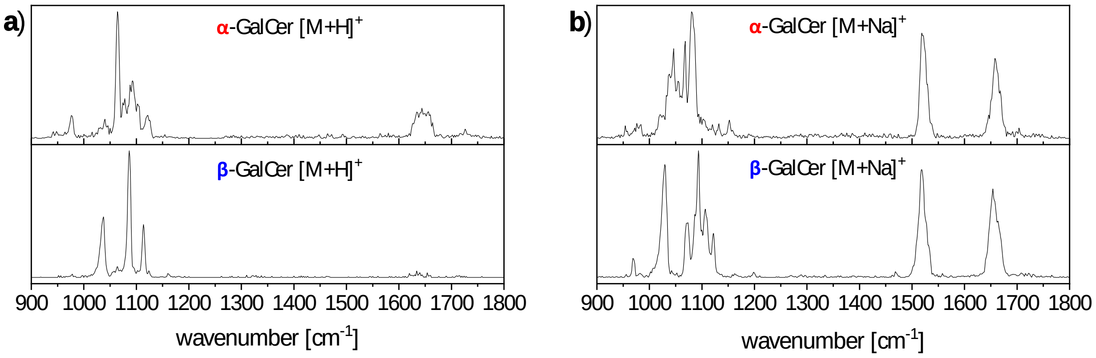

Fig. 1: IR spectra of protonated (a) and sodiated (b) α- and β-GalCer. The absorptions in the fingerprint region (950–1150 cm^{-1}) are diagnostic for the anomeric configuration.

1.2 Aim of this Thesis

The aim of this thesis is to determine which structural differences occuring in isomeric glycolipids can be distinguished by cryogenic gas phase IR spectroscopy and thereby to shed light on the poorly characterized gas phase structures of ionized glycolipids. Following the finding that isomeric α- and β-GalCer, which are indistinguishable by tandem MS and IM-MS, yield characteristic IR fingerprints, the study is extended to a larger collection of glycolipids in this work. The glycosphingo- and glycoglycerolipids provided by the group of Prof. L. Teyton (Scripps Research Institute, California, USA) allow to separately compare the influence of structural differences in the glycan structure, the lipid backbone and the configuration of the glycosidic bond on the three-dimensional gas phase structure and thus on the IR spectrum. The study is accompanied by IM-MS measurements and determination of collision cross sections.

Because the determination of double bond positions and configurations in aliphatic lipid chains is still not sufficiently or not at all addressed by standard analytical techniques in lipidomics research, a second project was launched in cooperation with the group of Prof. C. Arenz (Humboldt-Universität zu Berlin, Germany). They provided synthetic analogues of 1-deoxysphingosine that differ only in the position or configuration of the C=C double bond. Theoretical calculations from a previous study on protonated 1-deoxysphingosine isomers predicted a charge-olefin interaction between the NH_3^+ group and the double bond with a geometry depending on the double bond position.[7] Therefore, the location of the NH_3^+ bending mode in the IR spectrum might be indicative for the position and configuration of the double bond. This hypothesis was tested by cryogenic gas phase IR spectroscopy.

2. Fundamentals

2.1 Biological Relevance of Carbohydrates and Lipids

The central dogma of molecular biology formulated in 1958 by Francis H. Crick states that biological information is transferred unidirectionally from nucleic acids to proteins *via* the template-driven translation of a base sequence into an amino acid sequence.[8] However, this DNA-based paradigm is insufficient to explain the enormous complexity of cells arising from comparatively few genes because it ignores the importance of two major classes of biomolecules: carbohydrates and lipids.[9] During the revolution of molecular biology in the 1970s, glycomics and lipidomics lagged far behind genomics and proteomics. The common knowledge about carbohydrate functions was restricted to their primary roles as energy sources and structural components of nucleic acids or of bio-scaffolds in plants and insects without apparent biological activity.[9] Lipids were mainly regarded as energy storage and biologically inert constituents of cell membranes.[10] In the course of the last 30 years, it has become undisputed evidence that both classes of biomolecules fulfill much more complex functions in cells, especially in signaling and cell-cell communication – indispensable processes for the existence of multicellular organisms.[9–11] The coating of cell surfaces by complex glycans enables the cells to communicate with the extracellular matrix and with other organisms, e.g. in host-pathogen interactions.[9,12] Cellular signaling cascades often involve lipids acting as secondary messengers.[10] In addition to their ability to transfer information, carbohydrates and lipids are also at the origin of cellular complexity; glycosylation and lipidation are very common post-translational modifications, which add a level of complexity to the template-based, linearly assembled proteins. The attachment of a glycan or lipid changes the protein's physicochemical properties by altering protein folding, stability and solubility.[11,13] The structural modifications allow targeting the protein to different locations in the cell, anchoring of the protein in the cell membrane and recognition of the modified protein by receptors.[11,14] Glycosylation and lipidation patterns are not predictable from the genetic code because carbohydrates and lipids are secondary gene products resulting from the catalytical action of particular enzymes. Glycosyl transferases and glycosidases assemble and disassemble complex glycans and a variety of specific transferases transfer different lipid moieties.[14,15] These enzymatic pathways allow a large spatial and temporal flexibility of glycosylation and lipidation, depending on the state of development, differentiation and metabolic changes induced by certain diseases.[13,15] The non-template-driven assembly and the structural complexity of carbohydrates and lipids explain why studying the structures and functions of these biomolecules and of more complex biomolecular compounds such as glycoproteins or glycolipids is very tedious and requires the combination of different analytical technologies.

2.2 Glycolipids

Glycolipids are glycoconjugates in which a carbohydrate is linked to a hydrophobic moiety *via* a glycosidic bond.[16] They are omnipresent in the cell membranes of all kinds of organisms ranging from bacteria to vertebrates.[17] According to the structure of their lipid backbone, glycolipids are categorized into three main classes: glycosylphosphatidylinositols, glycoglycerolipids and glycosphingolipids (GSLs).[18] Glycosylphosphatidylinositols anchor proteins in the cell membrane and contain a highly conserved glycan linked to a phospholipid *via* the cyclic alcohol inositol. In glycoglycerolipids the glycan is covalently linked to the glycerol backbone of a diacylglycerol, and GSLs bear an amino alcohol, a so-called sphingoid base, as backbone (Fig. 2).[2]

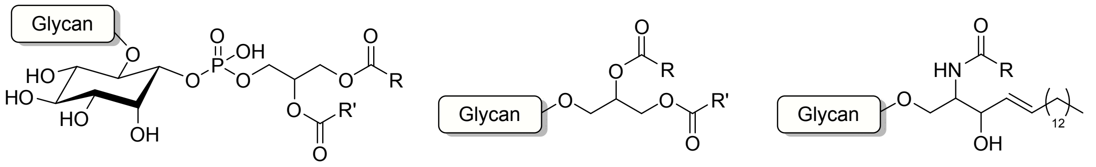

Glycosylphosphatidylinositol **Glycoglycerolipid** **Glycosphingolipid**

Fig. 2: Classification of glycolipids according to the structure of the lipid backbone. The core structures are phosphatidylinositol, glycerol and sphingosine. R and R' represent aliphatic chains of fatty acids.

In vertebrates nearly all glycolipids are GSLs.[17] GSLs belong to the broader class of sphingolipids, which were discovered by J. Thudichum in 1884.[19] This new class of complex lipids was named *sphingolipids* in allusion to the enigmatic sphynx from Greek mythology to refer to the sophisticated structure of sphingosine, which was not elucidated until 1947.[20] The modular structure of sphingolipids is composed of three distinct components: a sphingoid base bearing a variable headgroup and optionally an N-acyl-linked fatty acid (Fig. 3). The headgroup is either a simple hydroxy group in the case of ceramides or a more complex polar moiety such as a carbohydrate in the case of GSLs or a phosphate in the case of phosphosphingolipids. The configuration of the glycosidic bond between the sphingoid base and a chiral carbohydrate headgroup leads to stereoisomers. The sphingoid base is typically abbreviated by a shorthand nomenclature indicating the number of hydroxy groups (m = mono; d = di; t = tri), the number of carbon atoms and the number of double bonds, separated by a colon. The position and configuration of double bonds can be indicated in front. For example, the amino alcohol D-*erythro*-sphingosine (see Fig. 3), the most abundant sphingoid base in mammals, bears a C 18 chain with one *E*-configurated double bond between C 4 and C 5 and is thus abbreviated as 4*E*-d18:1.[20] The second most abundant sphingoid base in mammals is sphinganine, whereas phytosphingosine is mainly found in plants and fungi.[21] Phytosphingosine and sphinganine are derived from sphingosine by double bond hydration and hydrogenation respectively.

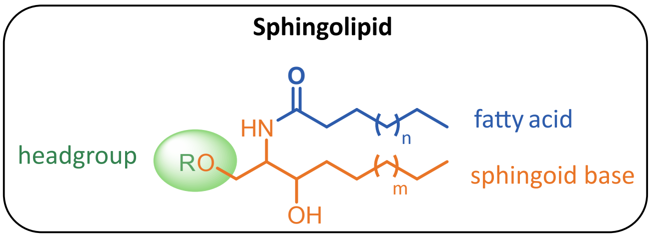

a) Classification by the headgroup R

Headgroup	Sphingolipid
H	Ceramide
Phosphate Phosphocholine Phosphoethanolamine	Phosphosphingolipid
Carbohydrate	Glycosphingolipid

b) Sphingoid bases

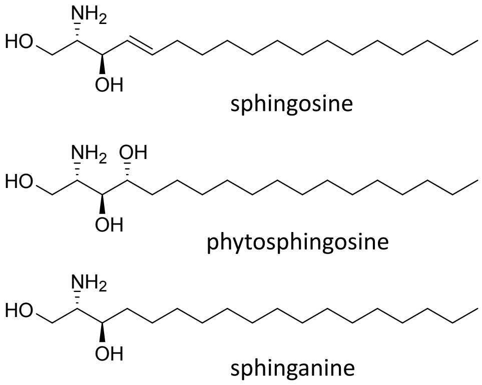

Fig. 3: Illustration of the modular structure of sphingolipids with different headgroups (a), sphingoid bases (b) and fatty acids. The common sphingoid bases sphingosine (4*E*-d18:1), phytosphingosine (t18:0) and sphinganine (d18:0) are shown.

Interestingly, GSLs are not essential for the survival of single cells but crucial for the development and function of multicellular organisms.[1,17] Owing to their amphiphilic nature, GSLs can easily insert into plasma membranes where their abundance varies between less than 5 % and more than 20 % of all membrane lipids in higher animals, depending on the cell type.[17] Being primarily located at the outer plasma membrane, they are involved in signaling processes and intercellular interactions.[22] GSLs preferentially accumulate with other membrane components such as cholesterol to form moving platforms, so-called lipid rafts, which play a role in membrane trafficking and signal transduction.[23,24] In the brain, GSLs such as GalCer are required for myelination of nerve cells to enable fast signal transduction.[25] Unusual levels of GSLs are indicative for several diseases including cancer, which is accompanied during its development by a dysregulation of the sphingolipid metabolism.[26] There also exist rare hereditary diseases resulting in a dysfunctional GSL metabolism, such as hereditary GSL storage diseases, in which GSLs accumulate in the lysosome as a result of defective enzymes required for their degradation.[2]

The biosynthesis of GSLs in mammals starts in the endoplasmic reticulum by the *de novo* synthesis of sphingoid bases. The backbone of sphingosine is formed by the condensation of L-serine and palmitoyl-CoA, which is catalyzed by serine palmitoyltransferase.[27] The following steps include the reduction of the ketone, N-acetylation and finally desaturation of the sphingoid base (Scheme 1).[28] The resulting ceramide can then be attached to a monosaccharide or phosphate headgroup to yield a GSL or phosphosphingolipid.[20]

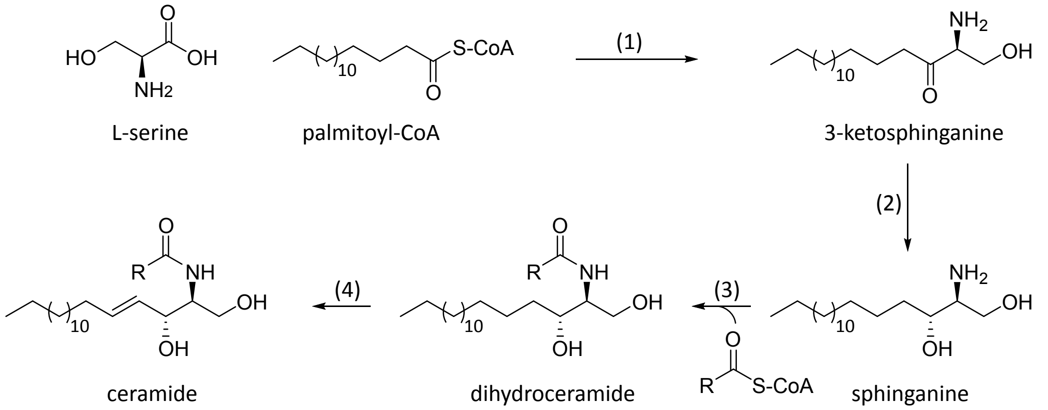

Scheme 1: Biosynthesis of ceramides in mammalian cells. The condensation of L-serine and palmitoyl-CoA is catalyzed by serine palmitoyltransferase (1) and yields 3-ketosphinganine, which is reduced (2) to yield the amino alcohol sphinganine. N-acetylation of sphinganine by a CoA-activated fatty acid (3) leads to a dihydroceramide, which is converted into a ceramide by dehydrogenation (4).

As a consequence of certain diseases such as the inherited neuropathy HSAN1, the substrate specificity of serine palmitoyltransferase can be shifted to favour L-alanine or glycine instead of L-serine (Scheme 2).[28] If L-alanine is used as substrate, the subsequent reaction cascade yields 1-deoxysphingolipids missing the primary hydroxy group; the analogous reaction with glycine leads to 1-(deoxymethyl)sphingolipids.[20] Contrary to normal ceramides bearing a 4*E* double bond, the predominance of *Z*-configurated double bonds between C 14 and C 15 was confirmed for 1-deoxyceramides.[29] As a consequence of those structural anomalies, the aberrant sphingolipids cannot be further metabolized to yield GSLs or phosphosphingolipids. Furthermore, they are not degradable *via* the canonical pathway, which requires phosphorylation of the 1-hydroxy group.[28,30] 1-Deoxysphingolipids thus tend to accumulate in HSAN1 patients where they have neurotoxic effects.[28] They were further identified as predictive biomarkers for type 2 diabetes mellitus.[31]

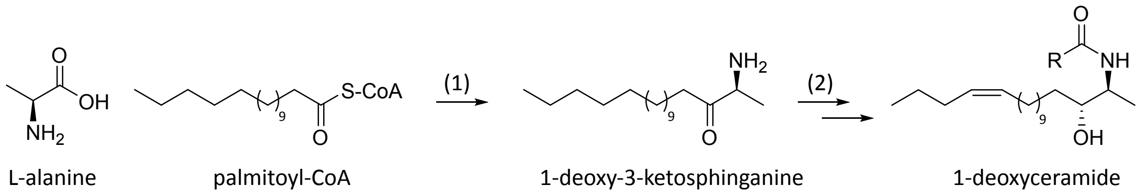

Scheme 2: Biosynthesis of 1-deoxyceramides. Serine palmitoyltransferase catalyzes the condensation of L-alanine and palmitoyl-CoA (1) to yield 1-deoxy-3-ketosphinganine. The substrate is converted into 1-deoxyceramide bearing a 14*Z* double bond *via* an alternative enzymatic pathway (2).

2.3 Structural Analysis of Glycolipids

Structure and function of glycolipids are tightly correlated; a minute structural difference such as the configuration of a glycosidic bond can be crucial for the biological activity (see Section 1.1). Studying glycolipids and their biological roles thus requires a comprehensive structure elucidation including regio- and stereochemical specifications. Current analytical techniques are confronted with several difficulties arising from the structural complexity and diversity of glycolipids. The glycan is the product of a non-template-driven synthesis performed by substrate-, regio- and stereoselective enzymes: glycosyltransferases and glycosidases.[32] The resulting linear or branched carbohydrates are composed of specific monosaccharide building blocks that are connected *via* glycosidic bonds with a defined regio- and stereochemistry. In glycolipids, the anomeric configuration of the reducing end is equally fixed. The variability of the lipid part is also important for the functionality of the molecule. Even though sphingosine is the predominant sphingoid base in mammalian GSLs, other less abundant sphingoid bases with varying chain lengths and with different numbers and positions of double bonds and hydroxy groups or even branched sphingoid bases exist in nature.[19] Furthermore, the length of the amide-linked acyl chain can vary from 14 to 26 or more carbon atoms, and the chain can contain α-hydroxy groups, C=C double bonds or other chemical modifications.[33] There is growing evidence that the positions of double bonds in lipids influence their biological functions and that lipid double bond isomers are involved in the development of several pathologies.[34] It is also important to note that the structural complexity of GSLs does not arise only from the diversity of the different components regarded separately but that the combinatorial biosynthesis of GSLs, i.e. the different possibilities to combine a sphingoid base, a fatty acid and a glycan, increases the pool of possible structures tremendously (Fig. 4).[22]

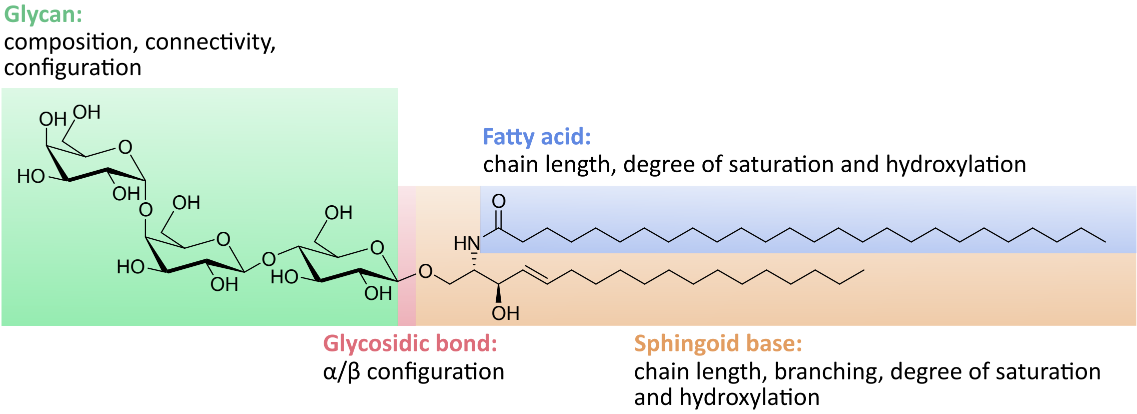
Glycan:
composition, connectivity, configuration
Fatty acid:
chain length, degree of saturation and hydroxylation
Glycosidic bond:
α/β configuration
Sphingoid base:
chain length, branching, degree of saturation and hydroxylation
OH
OH
O
HO
OH
O
OH
O
HO
OH
O
OH
O
HO
OH
O
O
HN
OH

Fig. 4: The structural complexity of GSLs (here β-Gb3 d18:1/26:0) arises from the structural diversity of the glycan and the lipid moieties and from their modular combination. The covalent attachment of a glycan to a sphingoid base results in a fixed stereochemistry of the interconnecting glycosidic bond.

The method of choice for the analysis of glycolipids is mass spectrometry (MS) in combination with electrospray ionization (ESI) or other soft ionization techniques. MS is often combined with chromatographic techniques such as thin-layer chromatography and liquid chromatography (LC), which are well suited for the separation of glycolipid mixtures.[17] Tissue imaging MS can be applied to locate different glycolipid species spatially in a biological sample and to relate them to the cell status.[33] The predominance of MS-based techniques in lipidomics and glycomics is justified by various reasons. The main advantages of modern mass spectrometers are a high mass accuracy, low detection limit and high sensitivity, which allow the detection of very small amounts of sample. MS can be used as a multichannel detector, which enables the detection of different glycolipids at a time and reveals low abundant species in the presence of highly abundant species in biological samples. Tandem MS experiments enable isolation of individual analyte ions to derive structural information *via* fragmentation. Despite all the advantages offered by MS, the technique suffers from an inherent drawback: exact chemical structures cannot be derived only from a mass-to-charge ratio (m/z). This is a major problem in the case of regio- and stereoisomers, which often occur particularly in the glycan part of glycolipids. The composition, connectivity and configuration of carbohydrates cannot be derived from the mass and in most cases, the fragmentation in tandem MS experiments does not yield diagnostic fragments either. For example, the comparatively simple isomeric glycolipids galactosylceramide and glucosylceramide are indistinguishable by tandem MS and the problem increases for larger glycans.[33] The lipid part also poses a problem; even though the chain lengths and degree of saturation can mostly be determined by tandem MS experiments, the position and configuration of double bonds remain unspecified. The comprehensive analysis of glycolipids thus requires the combination of MS with other techniques yielding complementary information.[35]

IMS is a gas phase separation technique that can be easily coupled to MS (see Section 2.4). In addition to the mass and charge, IM-MS also offers information about the size and shape of the ions, which allow to distinguish certain isomers. IM-MS was for example used for the analysis of a complex mixture of regioisomeric sialylated GSLs.[36] A recently emerged ultra-high resolution IMS technique providing separation pathlengths of tens of meters was even successfully employed to distinguish monosaccharides and certain kinds of lipid double bond regio- and stereoisomers.[18]

For the systematic determination of double bond positions, two conceptually different strategies have been developed: the direct derivatization of double bonds by chemical reagents or charge-switching methods based on adding positively charged species to carboxylic groups of free fatty acids and subsequent collision-induced dissociation (CID).[37] The derivatization of double bonds is more straightforward because it does not require prior release of the fatty acids from the lipid. A recent but now well-known MS-based technique following that approach is ozone-induced dissociation (OzID).[38] The ion-molecule reaction between unsaturated lipids and ozone is performed in an ion trap inside a mass spectrometer and therefore does not require chemical derivatization of the analyte. The addition of ozone is followed by chemically induced fragmentation of the ozonide yielding characteristic fragments that allow to determine the original position of the double bond. Yet, the applicability of OzID for stereoisomer identification remains rather limited because the distinction of Z and E double bond isomers only relies on different relative abundances of fragment ions and not on the formation of unique fragments.[39]

More detailed information about molecular structures including stereochemistry can be derived from spectroscopic techniques such as nuclear magnetic resonance (NMR) and IR spectroscopy. Both methods are directly structure-sensitive but not easily applicable to large biomolecules. NMR spectra get more intricate as the size of the molecule increases. The measurement requires milligrams of sample and due to its low sensitivity, NMR cannot detect small amounts of coexisting isomers.[40] In addition, NMR is a rather slow technique that measures the average of conformations adopted in solution; however, the investigation of conformational flexibility can be helpful for a better understanding of the biological functions of a molecule.[41] The conformational freedom of molecules can be explored by IR spectroscopy, which is sensitive to the spatial arrangement of atoms in their chemical environment. Consequently, the technique can be used to deduce information about functional groups, inter- and intramolecular interactions and distinct molecular conformations.[42] IR spectroscopy was employed in several studies for the investigation of glycolipid conformations and interactions in the condensed phase in relation to different physiological conditions such as temperature, pH and ion concentration.[43] In addition, the α- and β-anomer of a glycoglycerolipid, which form different crystalline structures, were distinguished by Fourier-transform IR spectroscopy.[44] However, the resolution of IR spectra of biomolecules in the condensed phase suffers from intermolecular interactions with the chemical environment and can be significantly enhanced by observing isolated species in the gas phase (see Section 2.5). The principles and applications of gas phase IR spectroscopy and IM-MS are detailed in the following.

2.4 Ion Mobility-Mass Spectrometry

IMS is an analytical technique used for ion separation in the gas phase based on the drift of ions under the influence of an electric field and in the presence of a buffer gas. Since the first report of the technique in 1898, various technical realizations based on the common principle of measuring ion mobilities in the gas phase have been developed.[45] One of the most popular techniques is drift tube (DT)-IMS.[46] The classical construction of a DT-IMS cell consists of stacked ring electrodes, which generate a constant and homogeneous electric field. The cell is filled with an inert gas such as helium or nitrogen. While the ions are accelerated by the electric field in the IMS cell, they undergo collisions with the buffer gas by which they are decelerated. The equilibrium between deceleration and acceleration on the molecular level results in a constant velocity of the ion on the macroscopic level.[47] The observable drift velocity v_d, which is given by the length l of the IMS cell divided by the measured drift time t_d of the ion, is proportional to the electric field E (Eq. 1). The proportionality constant K is the ion mobility, which is assumed to be independent of the electric field in DT-IMS.[45]

$$v_d = \frac{l}{t_d} = K \cdot E \tag{1}$$

K depends on the mass, charge, size and shape of the ion.[40] Smaller and more compact ions are less often decelerated by collisions than larger and more extended ions, and singly charged ions are accelerated less strongly by the electric field than multiply charged ions. The ion mobility is a measure of the collision frequency between the ions and the buffer gas and therefore depends on the temperature T and the pressure p in the IMS cell. The reduced mobility K_0 (Eq. 2) is normalized to standard conditions ($T_0 = 273.15\,\mathrm{K}$, $p_0 = 101325\,\mathrm{Pa}$) and allows for a better comparability between different experimental conditions, yet still depends on the temperature, the E/N ratio and the buffer gas.[45,47]

$$K_0 = K \cdot \frac{p}{p_0} \cdot \frac{T_0}{T} \tag{2}$$

The strength of DT-IMS compared to other IMS techniques relies on the possibility to convert ion mobilities directly into a rotationally averaged ion-neutral collision cross section (CCS) using the Mason-Schamp equation (Eq. 3).[45] Besides the reduced mobility K_0 the equation includes the ion charge z, the elementary charge e, the number density N_0 of the buffer gas at standard conditions, the reduced mass μ of the ion and a drift gas atom or molecule, the Boltzmann constant k_B and the temperature T. The CCS is an instrument-independent parameter, which can be stored in databases.[48]

$$\mathrm{CCS} = \frac{3ze}{16N_0}\sqrt{\frac{2\pi}{\mu k_B T}} \cdot \frac{1}{K_0} \tag{3}$$

IMS can be coupled to MS to add a second dimension of separation and characterization. The CCS provides a structural parameter related to the ion's size and shape, which allows to distinguish isomers with different shapes in the gas phase. Isomers of large biomolecules can be identified based on the CCSs of fragments.[40] The hyphenation of LC, IMS and MS provides complementary retention times, CCSs and m/z for the identification of isomeric species from complex mixtures.[49]

2.5 Gas Phase Infrared Spectroscopy

The irradiation of molecules with IR light excites molecular vibrations if the frequency of the incident IR radiation is resonant with IR active vibrational transitions. The frequency range in which particular mid-IR absorptions occur can be roughly predicted by the nature of the chemical bonds and functional groups; however, the local chemical environment of the vibrating atoms has a major influence on the exact frequency. This is why IR spectroscopy is a valuable tool to probe inter- and intramolecular interactions such as hydrogen bonds and electrostatic interactions to determine secondary structures and conformations.[42] To gain such in-depth structural information, experimental IR spectra are compared with computed IR spectra obtained from frequency analyses of structural candidates. Theoretical calculations on single molecules exclude intermolecular interactions and are thus not comparable with IR spectra of condensed molecules. Hence, the isolated molecule must be observed without the disturbing influence of its chemical environment to avoid for example inhomogeneous line broadening. Such a clean environment is provided by the gas phase.[50]

Gas phase IR spectroscopy can be performed either at ultra cold or finite temperatures. Spectroscopy at ultra cold temperatures holds the advantage that only the lowest energy conformations are populated, which leads to a significant decrease of spectral complexity.[50] If ions are observed instead of neutral molecules, technologies and devices developed for MS can be employed to guide the ions by electric and magnetic fields. The combination of MS, cryogenic techniques and IR spectroscopy thus provides a powerful setup for ion production, trapping and cooling followed by spectroscopic detection.[41] However, the technical realization of ultra cold gas phase IR spectroscopy of ions initially suffered from a severe problem: identical electrical charges repel each other and the space-charge limit restricts the ion densitiy in the gas phase to around 10^6 ions per cm^3.[50] For a reliable detection of light attenuation, which is measured in classical IR absorption spectroscopy, a minimal particle density of 10^{10} cm^{-3} is required.[51] The minimal particle density is derived from the Lambert-Beer law (Eq. 4), which expresses the intensity of transmitted light $I(\nu)$ of a specific frequency ν as a function of the intensity of the incident light I_0, the absorption cross section $\sigma(\nu)$, the pathlength l of the light traversing the sample and the particle density N.[52]

$$I(\nu) = I_0 \cdot e^{-\sigma(\nu) \cdot l \cdot N} \tag{4}$$

Ions in the gas phase are optically too dilute for measuring their impact on traversing IR light. Solutions to this problem are provided by different spectroscopic techniques embraced by the term *action spectroscopy.* Instead of measuring the impact of the ions on the light, action spectroscopy relies on measuring the impact of the light on the ions, for example by observing the yield of photofragmentation (Fig. 5). The number of unaffected

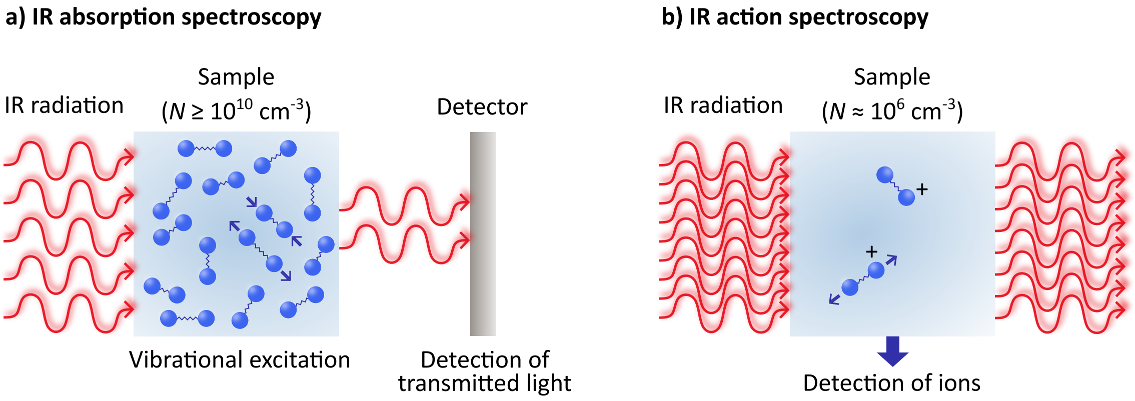

Fig. 5: Schematic illustration of the different principles underlying IR absorption spectroscopy and action spectroscopy. a) Absorption spectroscopy requires a high density ($N \geq 10^{10}$ cm^{-3}) of molecules whose impact on the light is measured. b) Action spectroscopy on gaseous ions usually requires a high photon density and the impact of the photons on the ions is observed.

ions $n(\nu)$ can be expressed depending on the number n_0 of precursor ions in a similar equation (Eq. 5) as the intensity of transmitted light is expressed by the Lambert-Beer law; however, the exponent no longer contains the particle density and pathlength but the photon fluence $F(\nu)$ of the IR source. The equation is only valid for a linear photon fluence dependency approach.[53]

$$n(\nu) = n_0 \cdot e^{-\sigma(\nu) \cdot F(\nu)} \tag{5}$$

Because the energy of one IR photon is much lower than the minimal energy required for the dissociation of a covalent bond, action spectroscopy is only possible if very weak, non-covalent bonds are present *or* if the IR source is powerful enough to enable the absorption of multiple photons by one single ion.[50] Two techniques pursuing either of these alternative strategies are IR messenger spectroscopy and IR multiple-photon dissociation (IRMPD) spectroscopy. Messenger spectroscopy relies on the capability of one single IR photon to dissociate weakly bound ion-molecule complexes (Fig. 6a).[51] The ion-molecule complex is initially formed by the condensation of a so-called messenger onto the ion at ultra cold temperatures by charge-induced dipole interactions. The messenger is usually a rare gas atom or molecular hydrogen or nitrogen to ensure a minimal influence on the IR spectrum due to the lack of intrinsic IR absorptions and weak interactions with the ion. Upon detachment of the messenger from the ion by photon absorption, the relative intensity of the ion-messenger complex in the mass spectrum decreases, whereas an increase of the isolated ion signal is observed.[54] The resulting IR spectrum resembles to a linear absorption spectrum because one photon is sufficient to initiate the dissociation of the non-covalent complex.[52]

IRMPD spectroscopy requires the absorption of multiple photons, which leads to a non-linear IR spectrum (Fig. 6b).[51] As in messenger spectroscopy, the yield of fragmentation induced by the absorption of IR photons is measured. The sequential absorption of multiple IR photons by molecular ions in the IRMPD process leads to thermal activation and finally cleavage of the weakest chemical bond. The fragmentation yield is monitored by MS to generate an IR spectrum. The quality of the obtained IR spectra suffers from several drawbacks such as broadening and red-shifting of vibrational bands and non-linear shifts of relative intensities.[50] These drawbacks are results of anharmonic coupling of vibrational modes at high internal energies; the excited vibrational level is rapidly depopulated by intramolecular vibrational redistribution (IVR), which dissipates the energy into other vibrational modes before the absorption of the next photon.[51] A large conformational freedom of the analyte ions also results in spectral congestion, especially if the spectra are recorded at room temperature without additional cooling.

Besides messenger spectroscopy and IRMPD, there exist other techniques to obtain IR spectra of ions in the gas phase. One of them is cryogenic gas phase IR spectroscopy in superfluid helium nanodroplets (Fig. 6c), which was initially developed for neutral molecules in the 1990s and extended to biomolecular ions in 2010.[55,56] This particular kind of IR spectroscopy combines the advantages of the gas phase and of classical matrix isolation. Superfluid helium possesses several unique properties that make it perfectly suitable as spectroscopic matrix.[57] First of all, helium is transparent over the whole spectral range from far IR to vacuum UV radiation. Clusters of superfluid helium readily pick up impurities and cool them down to the equilibrium temperature of 0.37 K.[57] Furthermore, the helium matrix does not disturb the vibrations of the embedded ion and hardly influences the vibrational frequencies because superfluid helium is only very weakly interacting and its viscosity is vanishingly small. The spectra obtained in the helium matrix are thus comparable to gas phase spectra of isolated ions.[58,59] The absorption of an IR photon by the ion is followed by vibrational relaxation leading to the evaporation of helium, which dissipates the thermal energy of the ion very fast. The process is repeated several times and therefore the ion returns into its vibrational ground state after each absorption of an IR photon. Hence, the helium matrix can be seen as a cryogenic IR-transparent thermostat keeping the ion at 0.37 K by evaporative cooling, thereby avoiding the increase of its internal energy. After the sequential absorption of multiple photons, the ion is released and detected by MS.[58] The IR spectra obtained by plotting the ion yield against the light frequency are highly resolved and not altered by red-shifts or band broadening as in IRMPD. Nonetheless, the presence of multiple conformers can still complicate the spectrum despite the low temperature close to the absolute zero point; multiple stable low-energy conformers can coexist or a higher-energy conformer can be kinetically trapped by the rapid cooling.[41] The trapping of higher-energy conformers can be restricted by cooling the ions prior to the pick-up process. The technical realization of IR spectroscopy in helium nanodroplets requires a very powerful and tunable mid-IR light source providing a high photon flux to enable the sequential absorption of multiple photons by a single ion. These requirements are met by IR free electron lasers (FELs), which employ relativistic electrons as the active lasing medium to generate intense IR radiation (see Section 3.3).[60] IR spectroscopy in helium nanodroplets using FEL-generated IR radiation was successfully applied to different biomolecules, e.g. for the differentiation of isomeric oligosaccharides,[42] the investigation of three-dimensional protein structures in the gas phase[52] and recently also for the differentiation of isomeric α- and β-galactosylceramides (see Section 1.1).

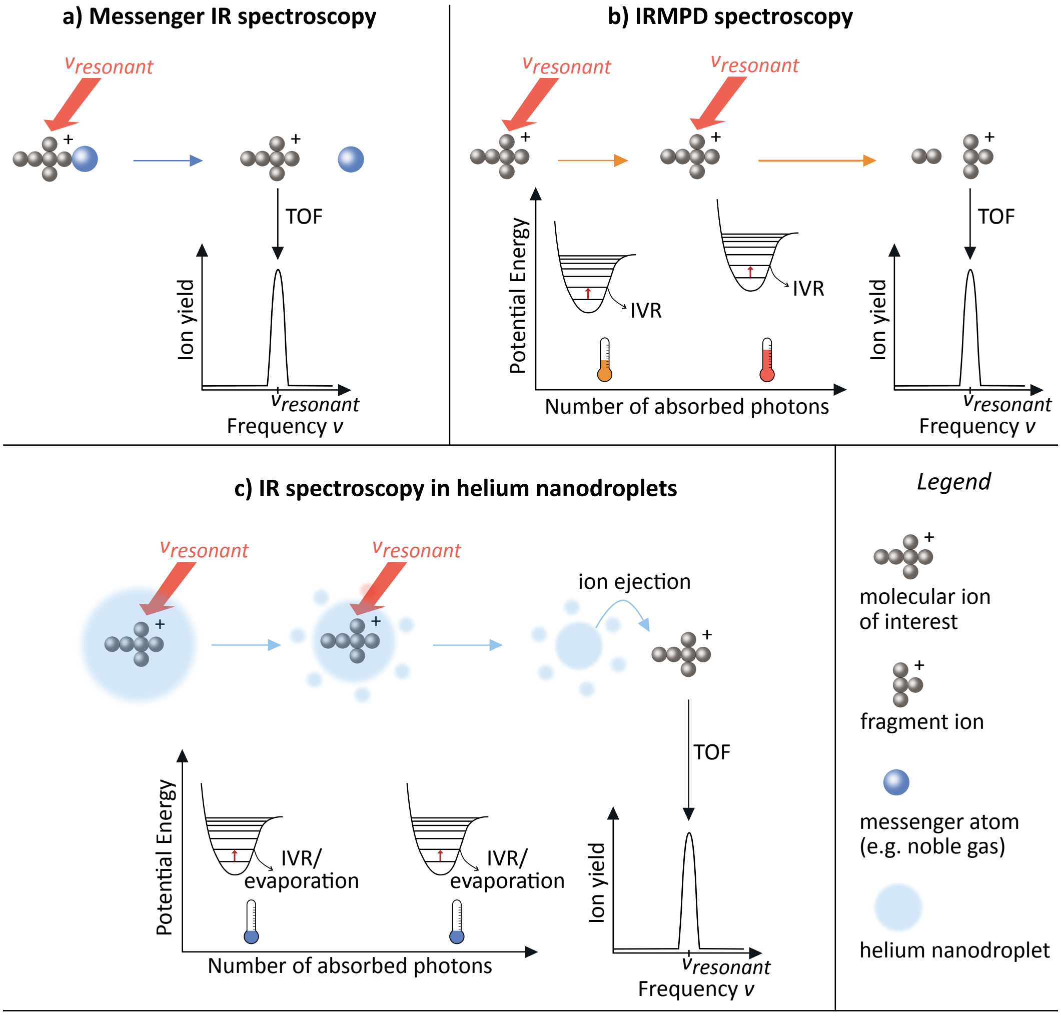
a) Messenger IR spectroscopy
$\nu_{resonant}$
+
TOF
Ion yield
$\nu_{resonant}$
Frequency ν
b) IRMPD spectroscopy
$\nu_{resonant}$
$\nu_{resonant}$
TOF
Potential Energy
IVR
IVR
Number of absorbed photons
Ion yield
$\nu_{resonant}$
Frequency ν
c) IR spectroscopy in helium nanodroplets
$\nu_{resonant}$
$\nu_{resonant}$
ion ejection
TOF
Potential Energy
IVR/ evaporation
IVR/ evaporation
Number of absorbed photons
Ion yield
$\nu_{resonant}$
Frequency ν
Legend
molecular ion of interest
fragment ion
messenger atom (e.g. noble gas)
helium nanodroplet

Fig. 6: Schematic overview of the principles underlying different gas phase IR spectroscopic techniques. a) Messenger IR spectroscopy: a non-covalent complex between the ion of interest and a messenger is dissociated upon IR absorption. b) IRMPD spectroscopy: absorption of multiple photons leads to an increase of the internal energy of the molecular ion until it dissociates. c) IR spectroscopy in helium nanodroplets: helium evaporates upon absorption of multiple IR photons by the ion and cools the embedded analyte until its release from the droplet.

3. Experimental Section

3.1 Sample Preparation

The synthetic glycolipids listed in table 1 were provided by the group of Prof. L. Teyton (Scripps Research Institute, California, USA) as solutions in dimethyl sulfoxide (1–15 mM). Samples **1a-d** and **2a/b** are monoglycosyl phytosphingosines bearing glucose (Glc), galactose (Gal) or glucuronic acid (GlcA) headgroups with different anomeric configurations. The samples **3a-d** correspond to the samples **1a-d** with phytosphingosine being exchanged for sphingosine. Samples **4a/b** are galactosylglycerolipid anomers and sample **5** is a globotriaosylceramide (Gb3) bearing a trisaccharide headgroup.

Tab. 1: List of glycolipid samples including structures, sum formulas, exact masses and specifications about the glycan and the lipid. Isomers are labeled with the same number and different letters.

Sample	Structure	Composition
Monoglycosyl phytosphingosines		
1a	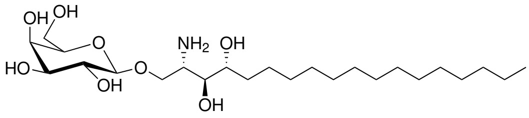	$C_{24}H_{49}NO_8$ exact mass: 479.35 u β-**Gal** t18:0
1b	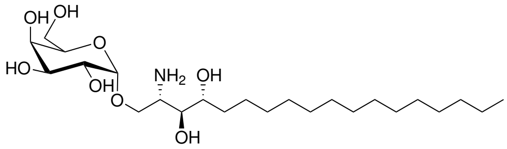	$C_{24}H_{49}NO_8$ exact mass: 479.35 u α-**Gal** t18:0
1c	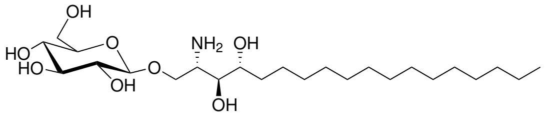	$C_{24}H_{49}NO_8$ exact mass: 479.35 u β-**Glc** t18:0
1d	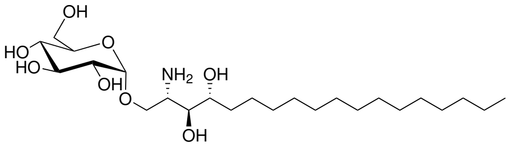	$C_{24}H_{49}NO_8$ exact mass: 479.35 u α-**Glc** t18:0
2a	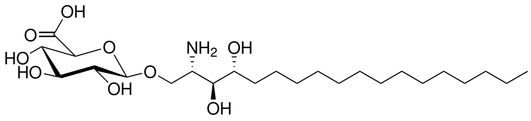	$C_{24}H_{47}NO_9$ exact mass: 493.33 u β-**GlcA** t18:0
2b	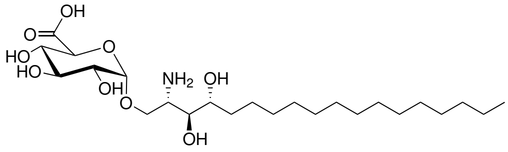	$C_{24}H_{47}NO_9$ exact mass: 493.33 u α-**GlcA** t18:0

Sample	Structure	Composition
Monoglycosyl sphingosines		
3a	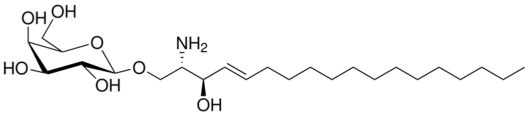	$C_{24}H_{47}NO_7$ exact mass: 461.34 u β-**Gal** 4*E*-d18:1
3b	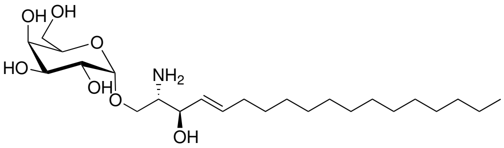	$C_{24}H_{47}NO_7$ exact mass: 461.34 u α-**Gal** 4*E*-d18:1
3c	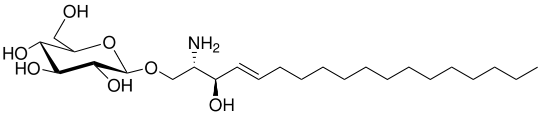	$C_{24}H_{47}NO_7$ exact mass: 461.34 u β-**Glc** 4*E*-d18:1
3d	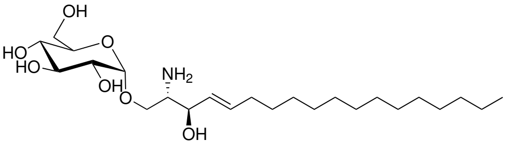	$C_{24}H_{47}NO_7$ exact mass: 461.34 u α-**Glc** 4*E*-d18:1
Glycoglycerolipids		
4a	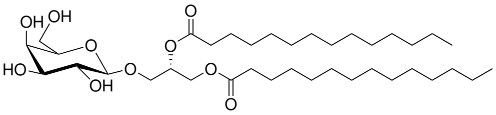	$C_{37}H_{70}O_{10}$ exact mass: 674.50 u β-**Gal** 14:0/14:0
4b	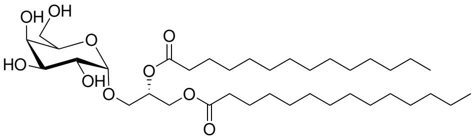	$C_{37}H_{70}O_{100}$ exact mass: 674.50 u α-**Gal** 14:0/14:0
Globotriaosylceramide		
5	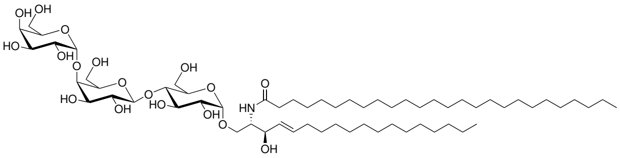	$C_{62}H_{117}NO_{18}$ exact mass: 1163.83 u α-**Gb3** 4*E*-d18:1/26:0

The glycolipids were diluted in a 1:1 (v:v) mixture of acetonitrile and chloroform to obtain 1 mM stock solutions. Prior to measurements, the stock solutions were diluted 1:10 and 1:100 in a 2:2:1 (v:v:v) mixture of acetonitrile, methanol and water to yield 100 µM and 10 µM solutions. Separate from this procedure, the GSL **5** was diluted from the stock solution using pure methanol. Silver adducts for IM-MS were prepared by mixing a 17 mM solution of $Ag[PF_6]$ in acetonitrile with 100 µM glycolipid solutions in a ratio of 1:10.

The 1-deoxysphingoid bases listed below (Tab. 2) were synthesized by the group of Prof. C. Arenz (Humboldt-Universität zu Berlin, Germany) following recently published synthetic routes.[29,61] Sample **6** is 1-deoxysphinganine, the 1-deoxy analogue of the saturated sphingoid base sphinganine. The 1-deoxysphingolipids **7a-e** are isomers of unsaturated 1-deoxysphingosine with varying double bond positions and configurations; the samples **7a-d** are double bond regioisomers and the sample **7e** is the configurational double bond isomer of sample **7d**. All samples were dissolved in methanol to obtain 10 mM stock solutions. For measurements, the stock solutions were diluted 1:100 and 1:1000 in methanol to obtain 100 µM and 10 µM solutions.

All solvents were purchased from Sigma-Aldrich. The solutions were stored at –32 °C. Chloroform-containing samples were stored in glass vials.

Tab. 2: List of 1-deoxysphingoid bases comprising 1-deoxysphinganine and 1-deoxysphingosine isomers including structures, sum formulas, exact masses and specifications about double bonds.

Sample	Structure	Composition
1-Deoxysphingolipids		
6	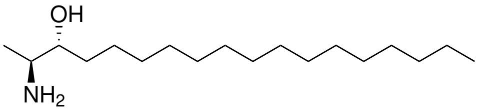	$C_{18}H_{39}NO$ exact mass: 285.30 u m18:0
7a	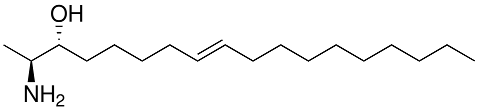	$C_{18}H_{37}NO$ exact mass: 283.29 u **8*E***-m18:1
7b	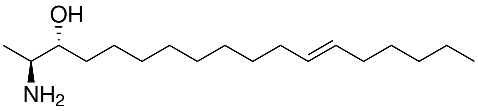	$C_{18}H_{37}NO$ exact mass: 283.29 u **12*E***-m18:1
7c	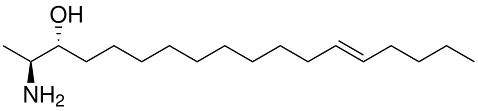	$C_{18}H_{37}NO$ exact mass: 283.29 u **13*E***-m18:1
7d	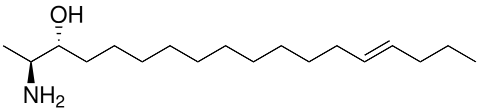	$C_{18}H_{37}NO$ exact mass: 283.29 u **14*E***-m18:1
7e	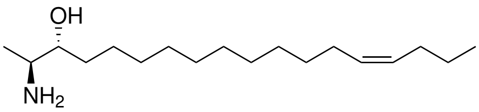	$C_{18}H_{37}NO$ exact mass: 283.29 u **14*Z***-m18:1

3.2 Ion Mobility Measurements

IM-MS measurements were performed on a Synapt G2-S HDMS instrument (Waters Corporation, Manchester, UK) using a nano-ESI source. The commercial instrument was modified by replacing the travelling-wave IMS cell by a drift tube (Fig. 7) .

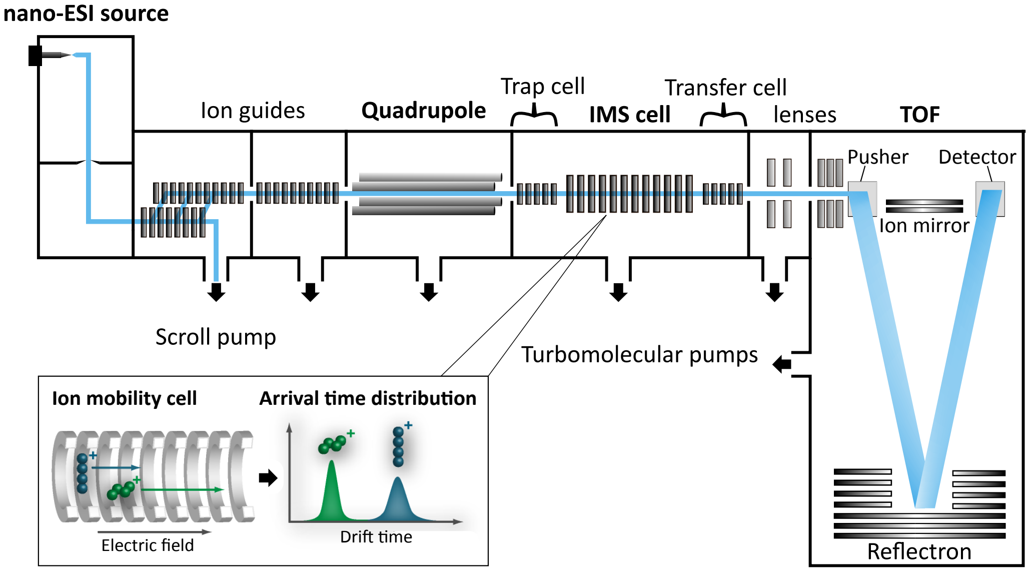
nano-ESI source
Ion guides
Quadrupole
Trap cell
IMS cell
Transfer cell
lenses
TOF
Pusher
Detector
Ion mirror
Scroll pump
Turbomolecular pumps
Ion mobility cell
Arrival time distribution
Electric field
Drift time
Reflectron

Fig. 7: Schematic setup of the modified Synapt G2-S HDMS ion mobility-mass spectrometer containing a drift tube ion mobility cell. The analytes are ionized by nano-ESI, followed by optional m/z selection in the quadrupole, ion mobility separation in the IMS cell and ion detection by time-of-flight (TOF)-MS. The correlation between ion shapes and drift times is shown at the bottom.

The ionization of dissolved analytes is performed by nano-ESI using home-made needles pulled from borosilicate capillaries by a P-1000 micropipette puller (Sutter Instrument, Novato, USA) and coated with palladium/platin by a sputter coater 108auto (Cressington, Dortmund, Germany). The samples were ionized from 10 µM solutions by applying a needle voltage of 0.6–0.8 kV. The ions enter the spectrometer following a Z-shaped pathway. A stepwave ion guide allows the rejection of neutrals and an efficient transfer of the ions to the quadrupole where they can optionally be m/z selected. Before the ions enter the drift tube, they traverse the trap cell where they can be fragmented by CID to perform ion mobility measurements of fragments. The ion mobility cell is filled with helium at a pressure of 2.2 Torr. The temperature of the drift tube is measured and noted before each measurement. After ion mobility separation, the ions are transferred into the TOF mass spectrometer *via* the transfer cell, which can be employed as a second collision cell. In this work, mass spectra were recorded in the m/z range from 100 to 2000 using the Sensitivity mode. Drift times were recorded for 60 seconds at 10 different drift voltages. The IMS Bias was varied between 50 V and 180 V while the other voltages were kept constant (Helium Cell DC = 60 V, Helium Exit = –40 V, Transfer DC Entrance = 5 V).

3.3 Cryogenic Gas Phase Infrared Spectroscopy in Helium Droplets

Cryogenic gas phase IR spectra were obtained using a home-built instrument that combines nano-ESI-MS and IR action spectroscopy in helium nanodroplets. The setup is devised to accomplish ion production, m/z selection, ion storage, ion pick-up by helium droplets and finally spectroscopic interrogation of the doped droplets followed by mass spectrometric ion detection. The essential components of the instrument are depicted below (Fig. 8). Technical details of the original instrument setup can be found elsewhere.[52]

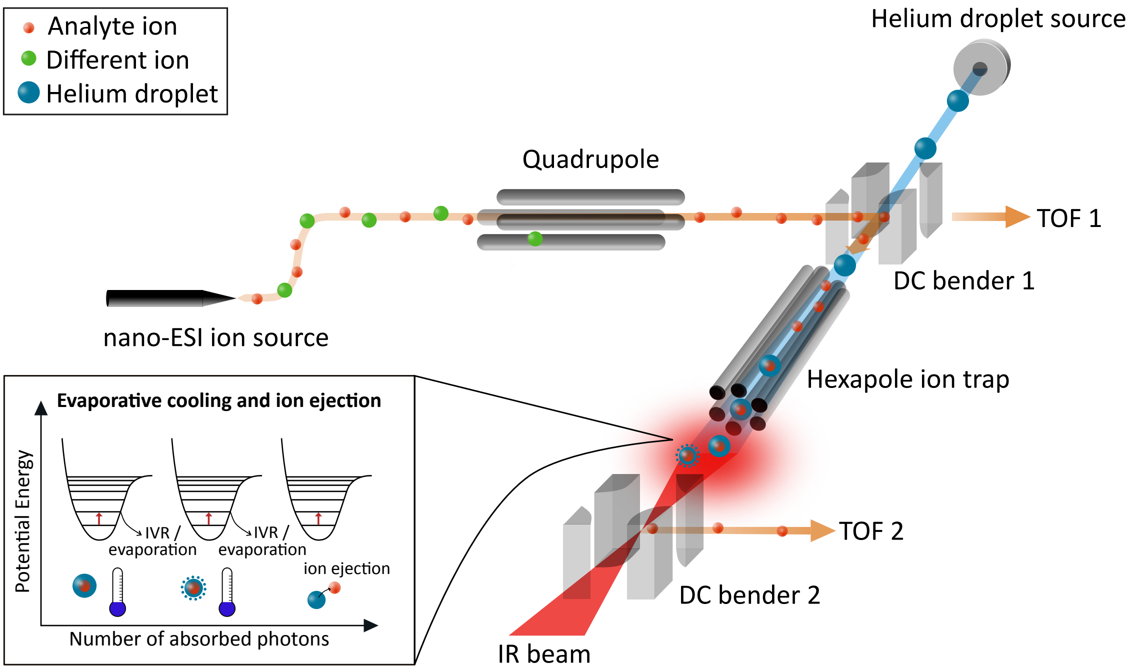
Analyte ion
Different ion
Helium droplet
Helium droplet source
Quadrupole
TOF 1
DC bender 1
nano-ESI ion source
Hexapole ion trap
Evaporative cooling and ion ejection
Potential Energy
IVR /
evaporation
IVR /
evaporation
ion ejection
Number of absorbed photons
TOF 2
DC bender 2
IR beam

Fig. 8: Schematic experimental setup for cryogenic gas phase IR spectroscopy in superfluid helium droplets. Ions are generated by nano-ESI, m/z selected in a quadrupole and trapped in a hexapole ion trap. A pulsed beam of helium droplets picks up the ions and the doped droplets leave the trap. Irradiation of the droplets with a pulsed IR beam from the tunable *Fritz Haber Institute* (FHI-)FEL leads to the evaporation of helium and finally to ion release and detection by TOF-MS.

The front end part of the instrument is built on the basis of a modified Q-TOF Ultima (Waters Corporation, Manchester, UK). For ionization by nano-ESI, either the commercial Z-spray source or a custom-made capillary source were employed. Ions were generated from 100 µM solutions by applying a needle voltage of ~ 0.8 kV. The ions are guided *via* two ion guides into high vacuum and to the quadrupole where they can be selected according to their m/z. The selected ions are then transferred through the non-operational collision cell into the first direct current (DC) bender. By applying a voltage to the bender, the ions are deflected by 90° and guided into a hexapole ion trap; otherwise, the ions travel straight into the first TOF mass spectrometer. The ion signal on the first TOF can be used to monitor the ion current from the nano-ESI source and optimize instrument parameters.

During the measurement of an IR spectrum, the voltage applied to the first bender is constantly switched on and off by a trigger system, which is coupled to the FEL pulse, the helium droplet source and the two mass spectrometers, to alternate between filling the ion trap and monitoring the quality of the ion signal. The deflected ions are trapped in the hexapole by a trapping potential of $\sim 3\,\mathrm{V}$ applied to the endcap electrodes and by radial confinement provided by a radio frequency waveform (1.1 MHz). The kinetic energy of the incoming ions is dissipated by collisions with helium buffer gas atoms. Before the ions are picked up by helium droplets, the buffer gas is pumped out after a short dwell time of about three seconds. The trap can also be cooled down to −190 °C by a flow of cold nitrogen gas through internal channels of the trap's copper housing. The nitrogen gas is externally cooled by liquid nitrogen.

Superfluid helium droplets are generated by the expansion of pressurized, highly purified helium into vacuum through a cooled nozzle (21 K), leading to an average droplet size of 10^5 helium atoms.[42] Helium atoms evaporate until the equilibrium droplet temperature of 0.37 K is reached. The helium droplets are pulsed at a rate of 10 Hz through a skimmer into the ion trap from which they can pick up ions. The kinetic energy of the doped helium droplets is high enough to overcome the potential barrier of the trap and travel towards the detection region. In the ion guide in front of the second bender, the droplets coincide with the pulsed IR beam generated by the FHI-FEL. The photon density can be adjusted by a variable focus mirror to yield a maximal ion signal without fragmenting the ion. In the case of resonant IR absorption by the analyte ion, helium evaporates until the bare ion is released (see Section 1.5). The ions are deflected by 90° by the second DC bender into the second TOF mass spectrometer. IR spectra are generated by scanning the spectral range of interest in steps of $2\,\mathrm{cm}^{-1}$ and by plotting the ion signal detected on the second TOF against the wavenumber. The data recorded during each measurement comprise the ion signals on both mass spectrometers as well as the actual wavenumber, the bandwidth and the energy of the FHI-FEL. Each IR spectrum was recorded at least twice to ensure reproducibility.

The FHI-FEL (Fig. 9) is a source for high energy, pulsed IR radiation that is characterized by a high photon density and narrow bandwidth.[60] The wavenumber can be continuously tuned over the whole mid-IR range from 3 µm to 60 µm. The active medium of the laser are electrons, which are released by a thermionic electron gun and accelerated by two linear accelerators until they reach a velocity close to the speed of light at an energy of 36 MeV. IR radiation is generated by injecting these relativistic electrons into a magnetic field created by permanent magnets of an undulator. The electrons are periodically deflected by the alternating magnets of the undulator and initially produce synchrotron radiation, which is monochromatic, yet incoherent. The interaction between the electron beam and the electromagnetic radiation in the cavity leads to self-amplification yielding monochromatic, coherent light. A small fraction of the light is out-coupled through a hole in one of the mirrors. The wavelength of the IR laser can be tuned by varying the magnetic field experienced by the electrons, which is accomplished by changing the gap of the undulator magnets. The output radiation is characterized by a well-defined time structure consisting of macro- and micropulses; the macropulses, which are 10 µs long and pulsed at a repetition rate of 10 Hz, contain 10^4 micropulses with a repetition rate of 1 GHz and a pulse width of 3–5 ps. For the measurement of IR spectra described above, 25 single shots (macropulses) of the FHI-FEL are used to obtain one datapoint. The energy of one macropulse ranges between 60 mJ and more than 100 mJ.

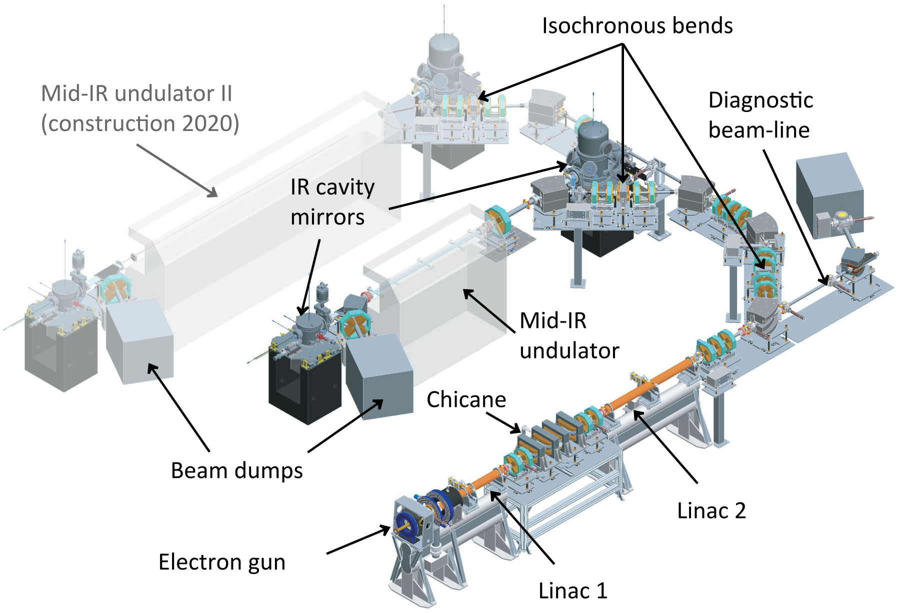

Fig. 9: Schematic setup of the FHI-FEL (taken from Ref. [60]). Electrons are liberated by the electron gun, accelerated by the two linear accelerators and injected into the mid-IR undulator. The laser light is generated in the cavity between the two cavity mirrors and the electrons are dumped.

3.4 Data Processing

Ion mobility data were processed using MassLynx (version 4.1, Waters Corporation). The drift peaks of the analyte ions were extracted from the arrival time distribution and exported to Origin (version 2018, OriginLab) to correct the drift times affected by asymmetric peak shapes. Each drift peak was fitted by a Gaussian and the center x_c of the fit function was read out as the corrected drift time. The procedure was repeated for all 10 individual drift peaks per measurement. CCSs were calculated by plotting the corrected drift times against the corresponding inverse drift voltages V_d and by fitting a linear fit function to the obtained data points. The formula for the linear fit is derived from the expression for the drift time t_d from eq. 1 and by taking into account the y-axis offset t_0 (Eq. 6).

$$t_d = \frac{l}{K \cdot E} + t_0 \tag{6}$$

By expressing the electric field E with the quotient of the drift voltage V_d and the length l of the drift tube, the proportionality relation between the drift times and the inverse of the drift voltages is obtained (Eq. 7).

$$t_d = \frac{l^2}{K} \cdot \frac{1}{V_d} + t_0 \tag{7}$$

The drift voltage V_d is composed of four different voltages, which can be individually set on the instrument. V_d is calculated from the Helium Cell DC, Helium Exit, IMS Bias and Transfer DC Entrance voltages according to eq. 8.

$$V_d = (\text{He Cell DC} + \text{He Exit} + \text{IMS Bias} - \text{Transfer DC Entrance}) \cdot \left(1 - \frac{2}{170}\right) \tag{8}$$

V_d was varied by varying only the IMS Bias to generate equidistant data points for the linear fit. The slope of the linear function obtained by plotting the drift times against the inverse drift voltages according to eq. 7 contains the ion mobility K, which can be converted into the reduced mobility K_0 and then into the CCS using the Mason-Schamp equation (Eq. 3). The conversion of K_0 into a CCS requires knowledge of the ion charge, the mass of the buffer gas and the temperature averaged from the 10 individual measurements. The CCS of each sample was calculated three times from measurements on different days and the error is given as the double standard deviation of the three CCS values rounded up to the next whole number.

IR spectra were generated by plotting the ion signal from the second mass spectrometer against the wavenumber of the FHI-FEL using Origin. For each final spectrum at least two individual spectra were averaged by normalizing the intensities of the individual spectra and generating an averaged spectrum with 1 datapoint per cm^{-1}. Spectra were only averaged if they were recorded with the same laser focus for comparability; however, the absorption intensities scale nonlinearly with absorption cross sections and with the laser energy, which can vary between different measurements and wavenumber ranges. Contrary to the absorption frequencies, which are not supposed to be affected by the multiple-photon absorption process, the relative intensities are thus of limited value and should not be overestimated; still, they can give a general idea about intensity differences.

4. Results and Discussion

4.1 Structural Diversity of the Glycan and Anomeric Configuration

The power of cryogenic gas phase IR spectroscopy to distinguish both isomeric glycans and anomeric configurations is demonstrated in the following using an exemplary set of monoglycosyl phytosphingosines bearing either Glc, Gal or GlcA headgroups with α- or β-anomeric configurations. A second example is given by the IR spectrum of α-Gb3 bearing a trisaccharide headgroup to illustrate the influence of the glycan size on the spectral quality.

4.1.1 Monoglycosyl Phytosphingosines

The isomeric monoglycosyl phytosphingosines **1a-d** consist of Glc or Gal linked to phytosphingosine *via* an α- or β-glycosidic bond. The two anomers **2a/b** complement set **1** by adding GlcA as a third headgroup leading to a mass difference of 14 u. The effects of the nature of the monosaccharide and anomeric configuration on the overall structure of the GSL ions in the gas phase and thus on the ion mobility and on molecular vibrations were investigated by DT-IM-MS and cryogenic gas phase IR spectroscopy in helium droplets.

The CCSs of protonated ions and of singly charged sodium and silver adducts of the monoglycosyl phytospingosines are listed in table 3, and the corresponding drift peaks of the isomers from set **1** are depicted below (Fig. 10). The CCSs of the $[M+H]^+$ and $[M+Na]^+$ ions of the different species are indistinguishable; the protonated α-isomers tend to exhibit slightly smaller CCSs than the β-isomers, but the difference is below 1 %. The addition of silver ions leads to an increase of the difference between α- and β-isomers; throughout all six molecules, the CCSs of silver adducts differ by 2 % depending on the anomeric configuration. The α-isomers adopt a slightly more compact shape than the β-isomers. This difference is significant but not sufficient to distinguish the anomers in a mixture. Interestingly, the CCSs increase upon the addition of sodium ions, whereas they decrease when silver ions are added (see Fig. 10d). This difference could be caused by a considerable conformational change of the molecule associated with the coordination of the relatively large silver ion, which is not induced by the addition of sodium ions. Both cations induce a slight broadening of the drift peaks compared to the drift peaks of the protonated species. The broader arrival time distribution could imply a larger conformational flexibility of the metal adducts arising from different possible coordination sites of the metal cation compared to the protonated species, in which the charge is very likely located on the primary amine. In any case, no difference was observed between the CCSs of Glc and Gal isomers. This result is in agreement with preceding ion mobility studies on small carbohydrates showing that the configuration of one hydroxy group of the monosaccharide does not significantly influence the ion mobility.[40]

Tab. 3: CCSs of $[M+H]^+$, $[M+Na]^+$ and $[M+Ag]^+$ ions of the monoglycosyl phytosphingosines **1a-d** and **2a**/**b** measured by DT-IM-MS in helium. The $^{DT}CCS_{He}$ values are given in Å^2 (± 1 Å^2).

Sample	$[M+H]^+$	$[M+Na]^+$	$[M+Ag]^+$
1a (β-Gal)	161	164	**156**
1b (α-Gal)	160	162	153
1c (β-Glc)	161	164	**157**
1d (α-Glc)	160	163	152
2a (β-GlcA)	161	163	**156**
2b (α-GlcA)	160	163	152

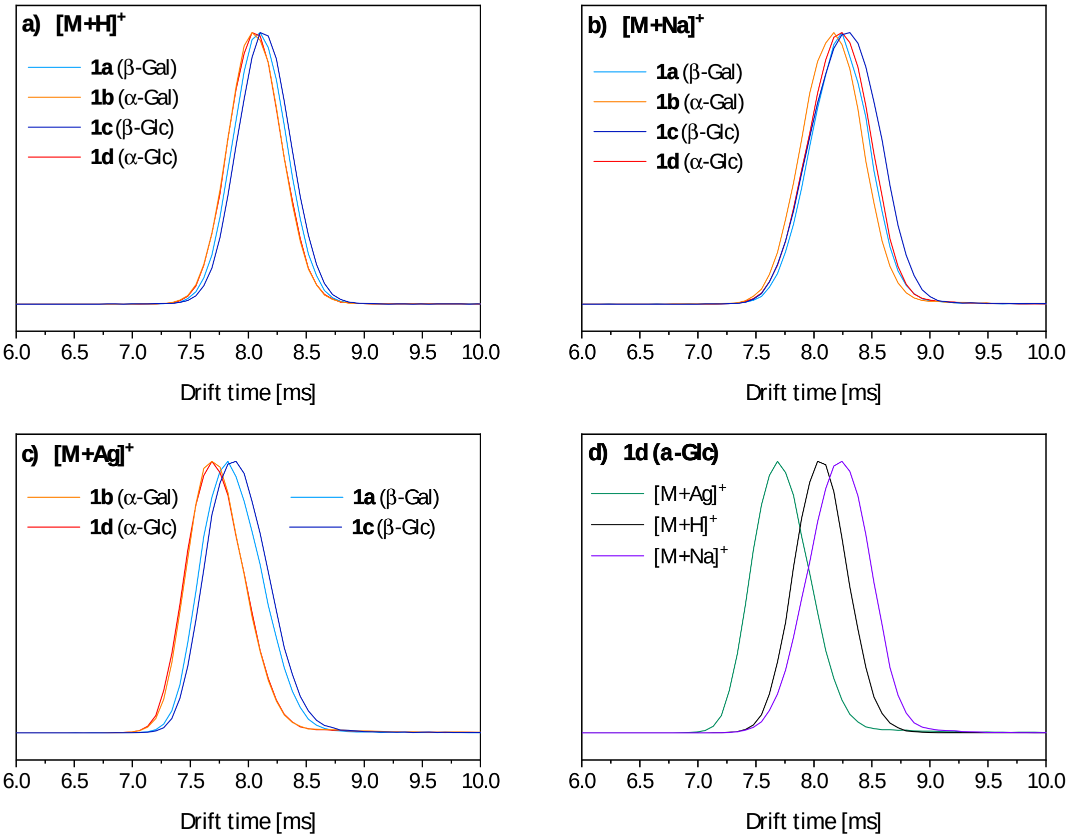

Fig. 10: Drift peaks of the isomeric monoglycosyl phytosphingosines **1a-d** attached to different cations. The samples are indistinguishable as $[M+H]^+$ ions (a) and $[M+Na]^+$ adducts (b); the drift peaks of the $[M+Ag]^+$ ions (c) are separated according to the anomeric configuration. The cation has a major influence on the drift time, as exemplarily shown for sample **1d** (d). The drift times were recorded at a constant voltage (IMS Bias = 50 V) and temperature (29.0 ± 0.5 °C).

In conclusion, DT-IM-MS is not sufficient to differentiate the four isomers **1a-d**; its applicability is restricted to the distinction of pure α- and β-stereoisomers as silver adducts. The analysis of anomeric mixtures is probably possible with a higher instrument resolution. However, the technique cannot be applied for the distinction of Glc and Gal isomers. The anomers **2a**/**b** are also only distinguishable as isomerically pure silver adducts.

Tandem MS experiments were performed using CID to derive more structural information about the isomers **1a-d**. The drift times of the resulting fragments were measured by DT-IMS. The main fragmentation pathway of the protonated ions and metal adducts consists in the cleavage of the glycosidic bond and consecutive elimination of water (Fig. 11). Consequently, the smaller fragments lack the monosaccharide headgroup, and the stereochemical information of the glycosidic bond is lost. The two fragments resulting from water loss from the parent ion (*m*/*z* 462 and 444) still carry the headgroup but their drift times are identical for all isomers. The mass of the low abundant fragment at *m*/*z* 360 corresponds to an X fragment resulting from cross-ring cleavage of the monosaccharide; however, the CCSs of the cross-ring fragments are identical for all four isomers (CCS = 142 ± 1 Å^2). Accordingly, the CCSs of all observed fragments are identical, independent of the monosaccharide and anomeric configuration, and therefore tandem MS does not contribute to the distinction of the isomers **1a-d**. The tandem MS spectra of the anomers **2a**/**b** also contain no information about the anomeric configuration.

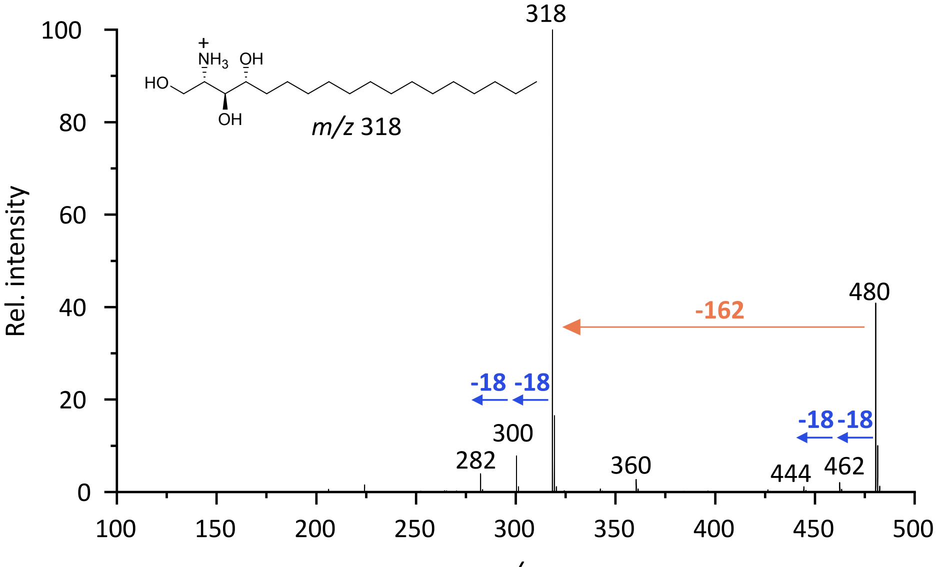

Fig. 11: Exemplary tandem MS spectrum of protonated α-galactosyl phytosphingosine **1b** obtained by CID (acceleration voltage = 18 V). The main fragment is protonated phytosphingosine (*m*/*z* 318) formed by glycosidic bond cleavage. Other fragments result from water elimination (-18) or from cross-ring cleavage (*m*/*z* 360). The spectra are identical for all isomers **1a-d**.

Cold-ion gas phase IR spectra of protonated monoglycosyl phytosphingosines were obtained in the spectral range from 900 cm^{-1} to 1800 cm^{-1} with additional cooling of the ion trap. The full scan spectra of the four isomers **1a-d** and the two anomers **2a**/**b** are shown below (Fig. 12). All spectra have in common a well-defined fingerprint region (1000–1150 cm^{-1}), whereas no strong absorption bands are present at higher wavenumbers except for the characteristic bands above 1700 cm^{-1} in the spectra of the samples from set **2**. In addition, weak absorptions with varying relative intensities are present in all spectra between 1400 cm^{-1} and 1500 cm^{-1}.

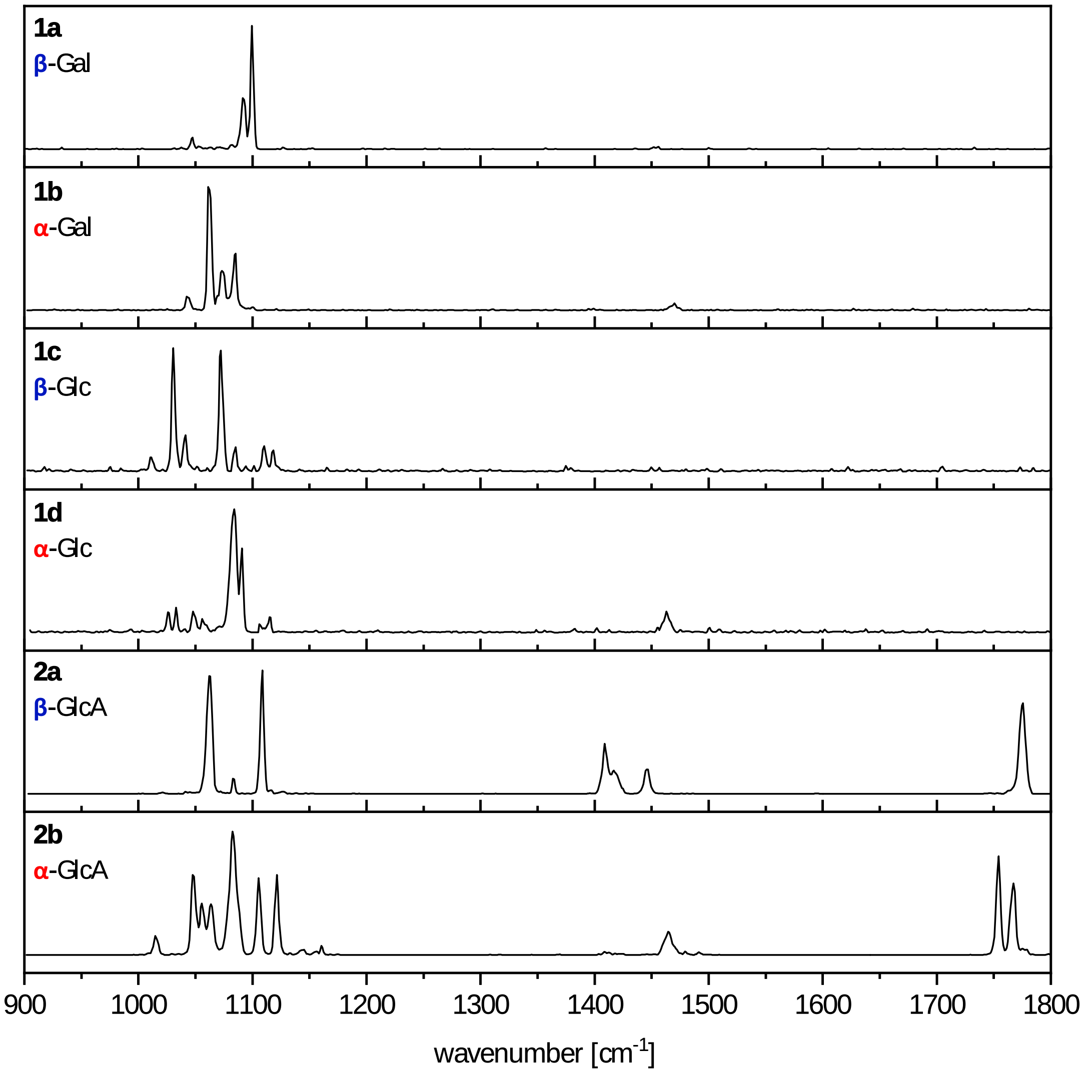

Fig. 12: Stacked IR spectra of protonated galactosyl, glucosyl and glucuronosyl phytosphingosines covering the spectral range from 900 cm^{-1} to 1800 cm^{-1}. The spectra exhibit strong, characteristic absorption bands in the fingerprint region (1000–1150 cm^{-1}) and weaker absorptions between 1400 cm^{-1} and 1500 cm^{-1}. The spectra of the glucuronosyl phytosphingosines (**2a**/**b**) display additional strong bands above 1700 cm^{-1}. All spectra were recorded while cooling the ion trap (-190 °C).

The IR spectra can be divided into three regions: the fingerprint region (1000–1150 cm^{-1}) characterized by strong absorption bands from coupled and anharmonic C−O and C−C stretching modes of the sugar ring,[62] the region of NH_3^+ bending vibrations (1400–1500 cm^{-1})[63,64] and the region of carbonyl stretching vibrations (1700–1800 cm^{-1})[64]. All three regions contain structural information.

The absorption pattern in the fingerprint region is unique for each combination of monosaccharide and anomeric configuration. The configuration of the glycosidic bond, the stereochemistry of one single hydroxy group at the C 4 carbon of the monosaccharide (Glc vs. Gal) and the presence or absence of a carbonyl group (Glc vs. GlcA) significantly alter the IR fingerprint. Because the overlap of absorption maxima is small between the different isomers, the monosaccharide and anomeric configuration can be unambiguously assigned by scanning only the spectral range from 1000 cm^{-1} to 1150 cm^{-1} (Fig. 13). Furthermore, it would be possible to detect a particular GSL in an isomeric mixture by monitoring the absorption at a unique wavelength, which does not excite the other isomers.

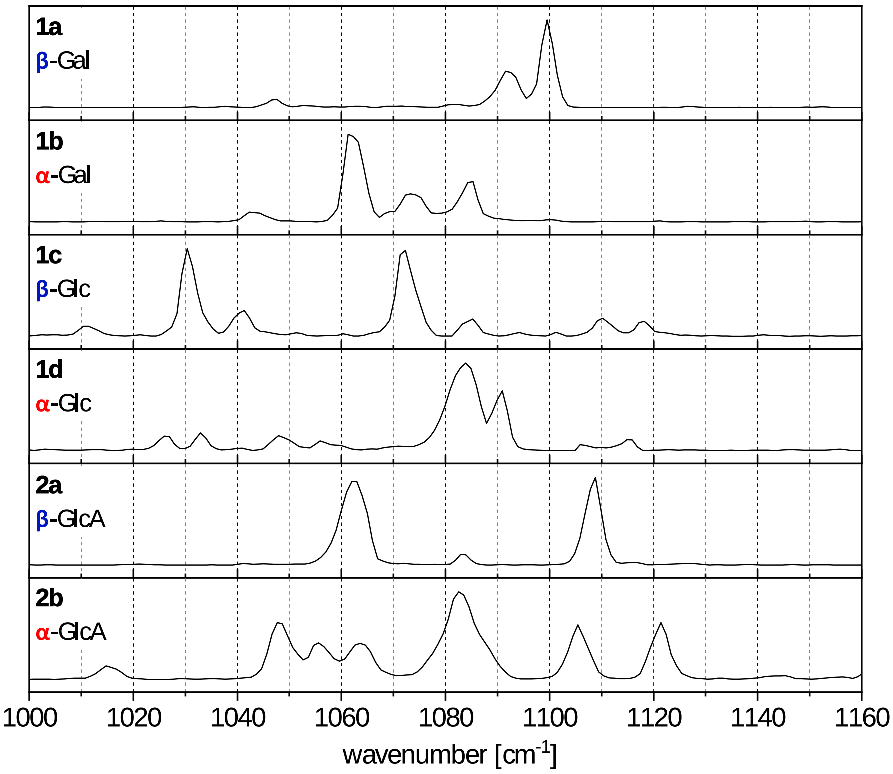

Fig. 13: Stacked IR spectra of protonated galactosyl, glucosyl and glucuronosyl phytosphingosines covering the fingerprint region (1000–1150 cm^{-1}). Each combination of monosaccharide and anomeric configuration yields characteristic absorption maxima. The spectra were recorded while cooling the ion trap (-190 °C).

The NH_3^+ umbrella modes of the protonated primary amines yield absorption bands between 1400 cm^{-1} and 1500 cm^{-1} but their intensity is very low compared to the bands of the fingerprint region in the spectra measured with a cooled trap. Interestingly, the relative intensity of the N−H bending vibrations could be significantly increased for almost all samples by keeping the ion trap at room temperature (Fig. 14).

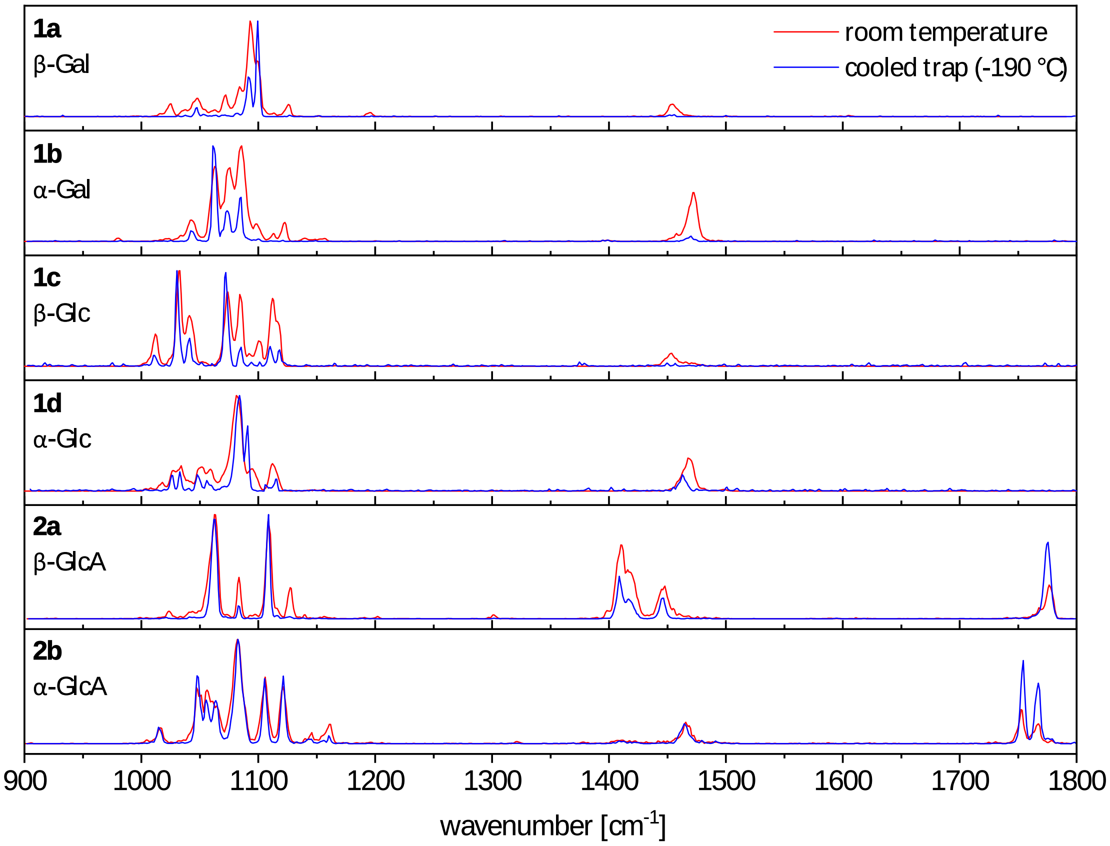

Fig. 14: Stacked IR spectra of protonated galactosyl, glucosyl and glucuronosyl phytosphingosines covering the spectral range from 900 cm^{-1} to 1800 cm^{-1}. The spectra were obtained without cooling the ion trap (red traces) or with cooling (blue traces). Without cooling, the absorption bands are broadened and the relative intensities of the NH_3^+ umbrella vibrations (1400–1500 cm^{-1}) are increased.

The ions entering the ion trap are thermalized by collisions with the buffer gas before being picked up by helium droplets. If the buffer gas is not cooled by liquid nitrogen, higher-energy conformers of the analyte ions can be thermally populated in the trap. Upon pick-up by helium droplets, the ions are rapidly cooled down to 0.37 K and therefore, the higher-energy conformers can be kinetically trapped. Hence, the IR spectra reflect different distributions of conformers depending on whether the trap was cooled or not. The coexistence of different conformers with similar energies leads to a slight broadening of absorption bands and shifts of relative absorption intensities in the spectra obtained without cooling. In some cases, additional bands of conformers that are absent in the cold trap appear. The spectra of the monoglycosyl phytosphingosines are only minimally altered by the increase of temperature and still well-resolved. The increased relative intensities of the NH_3^+ bending vibrations at room temperature may be explained by kinetic trapping leading to a higher ratio of conformers in which the vibration is not weakened or suppressed, e.g. by intramolecular interactions.

The higher relative intensities of the absorption bands between 1400–1500 cm^{-1} obtained without cooling the ion trap allow a comparison of their exact positions (Fig. 15). Apparently, the absorption frequencies are mainly determined by the anomeric configuration; the spectra of the α-isomers **1b** and **1d** exhibit absorption bands around 1470 cm^{-1}, whereas the position of the bands is shifted to 1450 cm^{-1} for the β-isomers **1a** and **1c**. The isomers from set **2** show a similar behaviour; the α-isomer absorbs at wavenumbers above 1460 cm^{-1} and the absorption band of the β-isomer is shifted to considerably lower wavenumbers below 1450 cm^{-1}. The spectrum of the β-isomer exhibits additional absorption bands in the region from 1400 cm^{-1} to 1430 cm^{-1}, which are also present but very weak in the spectrum of the α-isomer. These absorption bands are probably arising from C−O−H bending vibrations of the carboxyl group, which is only present in the samples **2a**/**b**.[64] Quantum chemical calculations will be required to assign the absorption bands more reliably to functional groups.

In conclusion, the NH_3^+ bending vibrations depend on the temperature of the buffer gas in the trap, which influences the relative absorption intensity, and on the anomeric configuration determining the absorption frequency. The intensity differences between the different samples are of limited relevance, because they mainly arise from the different intensities in the fingerprint region, based on which the rest of the spectrum is scaled.

In the spectra of the anomeric glucuronosyl phytosphingosines from set **2**, the spectral region above 1700 cm^{-1} is governed by C=O stretching vibrations of the carboxyl group. The frequency of C=O stretching vibrations depends on the chemical environment of the carbonyl group and is very structure-sensitive.[62] The absorption band appears at 1775 cm^{-1} in the case of β-GlcA (**2a**), whereas the α-isomer (**2b**) exhibits two bands at 1754 cm^{-1} and at 1767 cm^{-1}. The presence of two well-defined bands suggests the coexistence of at least two conformers in the spectrum of α-GlcA phytosphingosine, independent of the temperature in the ion trap. Both absorption bands are clearly different from the band of the β-isomer, so that α- and β-GlcA phytosphingosines can be distinguished not only by scanning the fingerprint region but alternatively also by scanning the region of carbonyl stretching vibrations (1700–1800 cm^{-1}).

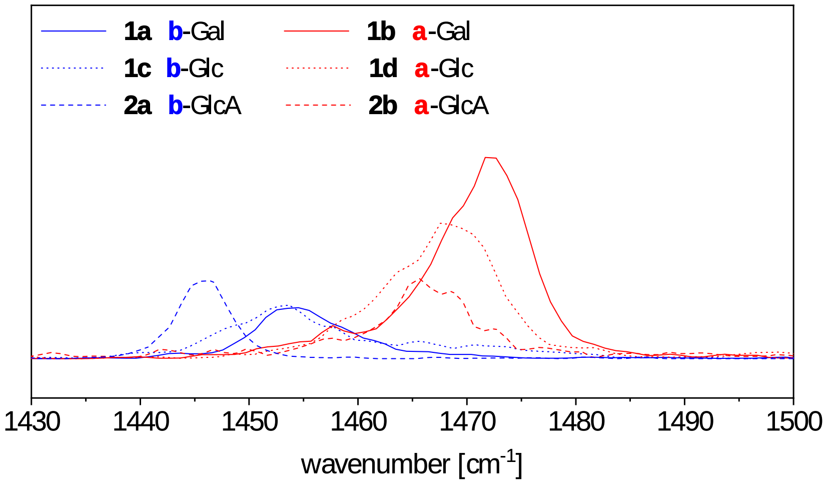

Fig. 15: Comparison of the absorption frequencies of the NH_3^+ bending modes in the spectra of α- and β-monoglycosyl phytosphingosines obtained without cooling the ion trap. The bands are shifted to higher wavenumbers in the spectra of the α-isomers compared to the β-isomers.

4.1.2 Globotriaosylceramide

Globotriaosylceramides are GSLs in which a ceramide is attached to a trisaccharide composed of a conserved monosaccharide sequence: α-D-Gal-(1→4)-β-D-Gal-(1→4)-D-Glc. In the Gb3 **5**, the trisaccharide is linked *via* an α-glycosidic bond to sphingosine, which is N-acetylated by a saturated fatty acid (26:0). The molecule is more complex than the monoglycosyl phytosphingosines on two different levels: it bears a trisaccharide instead of a monosaccharide headgroup and the lipid moiety is a ceramide instead of a bare sphingoid base. The influence of the glycan size on the fingerprint region of the gas phase IR spectra was tested by comparing the fingerprints of monosaccharides and of the trisaccharide of Gb3 to conclude if the absorptions of the trisaccharide are still resolved enough to be of diagnostic value.

Gas phase IR spectra of $[M+H]^+$ and $[N+Na]^+$ ions were recorded in the spectral range from 900 cm^{-1} to 1800 cm^{-1} (Fig. 16). In both spectra, the absorption pattern in the fingerprint region of α-Gb3 is still well-resolved and displays distinct, diagnostic features that contain structural information; nevertheless, the absorption bands are no longer baseline-separated as in the spectra of monoglycosyl phytosphingosines. The trisaccharide absorbs IR radiation in the whole range from 1000 cm^{-1} to 1150 cm^{-1} and as a consequence, the detection of α-Gb3 in a mixture of GSLs is no longer possible by relying on the absorption at one particular wavelength. The corresponding β-anomer was not available for comparison but it is very probable that its IR spectrum also exhibits a unique absorption pattern in the fingerprint region allowing to distinguish α- and β-Gb3.

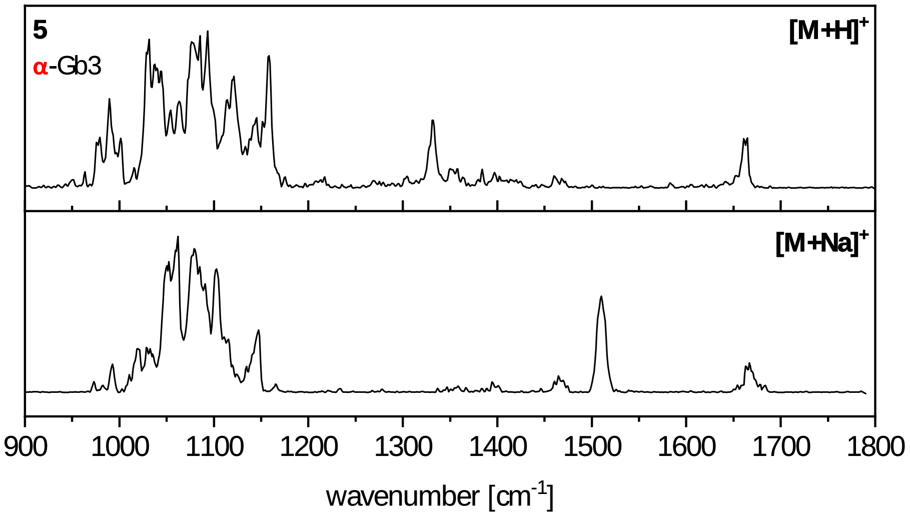

Fig. 16: IR spectra of protonated and sodiated α-Gb3 (**5**) in the spectral range from 900 cm^{-1} to 1800 cm^{-1}. The fingerprint region is more congested than the fingerprint regions of monoglycosyl sphingolipids but still well-resolved. The spectral range above 1500 cm^{-1} is governed by amide vibrations of the ceramide, which are influenced by the nature of the coordinating cation. The spectra were recorded while cooling the ion trap (-190 °C).

The spectral range above 1500 cm^{-1} is governed by vibrations of the amide. The amide I vibration (C=O stretching) is located between 1650 cm^{-1} and 1700 cm^{-1} and the amide II vibration (N−H bending) appears at lower wavenumbers between 1500 cm^{-1} and 1530 cm^{-1}. The coordinating cation was found to influence not only the absorption pattern in the fingerprint region but also the relative intensities of the amide vibrations. The amide I and amide II vibrations are intense in the spectrum of sodiated α-Gb3, whereas the N−H bending vibration is suppressed in the spectrum of the protonated species. The same observation was made for GalCer (see Fig. 1). In the case of α- and β-GalCer, the absorption frequencies of the amide vibrations are independent of the anomeric configuration. The IR spectrum of β-Gb3 will be measured to test the effect of the anomeric configuration on the amide vibrations in the case of Gb3.

In conclusion, gas phase IR spectroscopy yields well-resolved spectra of α-Gb3, which bears two lipid chains and a trisaccharide headgroup. However, the fingerprint region is more congested than the fingerprints of smaller monoglycosyl phytosphingosines bearing only one lipid chain and a monosaccharide headgroup. The increase of spectral congestion upon increasing the glycan size suggests that there is a size limit beyond which gas phase IR spectra are of limited value for structural assignment. In the case of large glycolipids, fragmentation of the oligosaccharide may be necessary prior to spectroscopic interrogation.

4.2 Structural Diversity of the Lipid

Structural variations of the lipid part were investigated by comparing glycolipids with different lipid backbones and Glc or Gal headgroups. The influence of a very small structural difference was tested by comparing monoglycosyl phytosphingosines and sphingosines, which can be interconverted by the addition or elimination of water. The comparison was extended to glycoglycerolipids, which are based on a fundamentally different lipid core structure. Finally, lipid double bond isomers were investigated using a set of 1-deoxysphingolipids.

4.2.1 Monoglycosyl Sphingosines

The set of monoglycosyl sphingosines (**3a-d**) comprises four isomers differing by the monosaccharide (Glc or Gal) and the anomeric configuration (α or β). The difference compared to the samples from set **1** consists in the exchange of phytosphingosine for sphingosine and a resulting mass difference of 18 u. The CCSs of the monoglycosyl sphingosines were determined by DT-IM-MS under the same conditions as the corresponding monoglycosyl phytosphingosines from set **1**. The results are given below (Tab. 4).

Tab. 4: CCSs of $[M+H]^+$, $[M+Na]^+$ and $[M+Ag]^+$ ions of the monoglycosyl sphingosines **3a-d** measured by DT-IM-MS in helium. The $^{DT}CCS_{He}$ values are given in $Å^2$ ($\pm$ 1 $Å^2$).

Sample	$[M+H]^+$	$[M+Na]^+$	$[M+Ag]^+$
3a (β-Gal)	153	158	150
3b (α-Gal)	154	157	151
3c (β-Glc)	152	157	153
3d (α-Glc)	153	158	150

The CCSs of protonated and sodiated monoglycosyl sphingosines (**3a-d**) are 4–5 % smaller than those of the corresponding monoglycosyl phytosphingosines from set **1** (see Tab. 3). This result is in agreement with the general observation made for different lipid classes that the introduction of a double bond into a hydrocarbon chain leads to a more compact shape of the molecular ion in the gas phase.[7,49] The drift times of protonated and sodiated monoglycosyl sphingosines do not allow any distinction between anomers or different monosaccharides (Fig. 17a). Contrary to the monoglycosyl phytosphingosines, the trend towards smaller CCSs of protonated α-anomers compared to the corresponding β-anomers is not observed for the monoglycosyl sphingosines; moreover, the separation of anomers could not be achieved by the addition of silver ions. The drift times of the silver adducts of all monoglycosyl sphingosines except for sample **3c** (β-Glc) are identical, whereas the drift time of the latter is slightly increased (Fig. 17b). According to the results obtained for the monoglycosyl phytosphingosines, sample **3a** (β-Gal) should equally exhibit a larger CCS than the α-anomers. The exchange of phytosphingosine for sphingosine obviously leads to different ion mobility trends of the samples from set **1** compared to set **3**, which indicate that silver ions coordinate to the molecules in different manners depending on the nature of the sphingoid base. Studies on phosphatidylcholines have previously shown that Ag^+ ions preferentially coordinate C=C double bonds in lipid chains,[65] which could be the case in monoglycosyl sphingosines. Owing to the lack of double bonds in monoglycosyl phytosphingosines, the silver ion is probably located at a different position. It may for example coordinate several hydroxy groups of the monosaccharide. Theoretical calculations are required to underpin these assumptions and to explain the aberrant behaviour of sample **3c**. It is possible that the coordination of Ag^+ leads to a particular conformation of sample **3c**, which is not adopted by the other isomers due to different molecular geometries. In any case, the CCSs of silver adducts listed in Tab. 4 are very close to the corresponding silver adducts of the α-configurated monoglycosyl phytosphingosines **1b** and **1d**. In accord with the IMS measurements of monoglycosyl phytosphingosines, the addition of sodium cations leads to an increase of CCSs, whereas the CCSs of silver adducts are decreased compared to the protonated species; however, the decrease of CCSs upon addition of silver ions is not as significant as in the case of monoglycosyl phytosphingosines, and the CCS of sample **3c** (β-Glc) even increases minimally when silver is attached to the molecule instead of a proton.

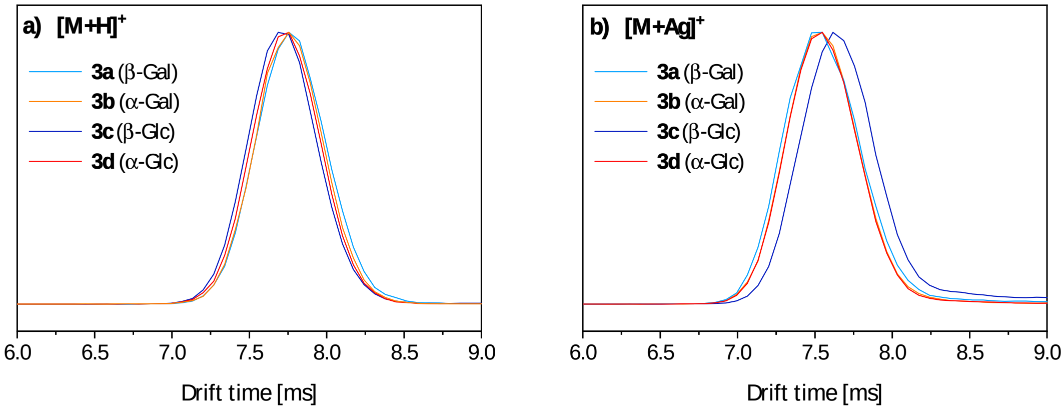

Fig. 17: Drift peaks of monoglycosyl sphingosines **3a-d** as protonated ions and silver adducts. The drift times of the $[M+H]^+$ ions are identical for all samples (a); the mobility of the $[M+Ag]^+$ ion of sample **3c** differs from the other samples (b). The drift times were recorded at the same voltage (IMS Bias = 50 V) and temperature (27.5 ± 1.0 °C)

In conclusion, DT-IM-MS does not yield valuable information for the distinction of the isomers **3a-d**. The CCS differences are around 1 %, which is within the error limits of the measurement; nevertheless, the different ion mobility trends of monoglycosyl sphingosines and phytosphingosines give hints about a conformational change of the molecules upon exchange of the sphingoid base. In a different study, β-Glc and β-Gal sphingosine (**3a** and **3c**) could be distinguished in a mixture with a very poor signal-to-noise ratio after a separation pathlength of 60 m using ultra-high resolution IM-MS,[18] indicating that the isomers **3a-d** might be distinguishable by other high-resolution IMS techniques.

Fragmentation of metal adducts and protonated monoglycosyl sphingosines by CID yielded fragments resulting from the cleavage of the glycosidic bond and elimination of water (Fig. 18). All fragments except for the fully dehydrated sphingoid base (m/z 264) are equally present in the tandem MS spectra of the monoglycosyl phytosphingosines from set **1** (see Fig. 11); however, whereas protonated phytosphingosine is the main fragment of the protonated samples **1a-d**, protonated sphingosine (m/z 300) is not abundant in the tandem MS spectra of samples **3a-d**. The ions instead undergo water elimination to yield dehydrated sphingosine (m/z 282). This ion can eliminate one more water molecule, which is not observed in the spectra of the monoglycosyl phytosphingosines. Cross-ring fragments were not formed upon fragmentation of the monoglycosyl sphingosines. The observed fragments contain no information about the monosaccharide and its anomeric configuration; the smallest fragments (m/z 282 and 264) lack the monosaccharide headgroup, and the drift times of the only fragment still bearing the monosaccharide (m/z 444) are identical for all isomers **3a-d**. Neither DT-IM-MS nor tandem MS are thus suitable techniques for the distinction of the isomeric monoglycosyl sphingosines from set **3**.

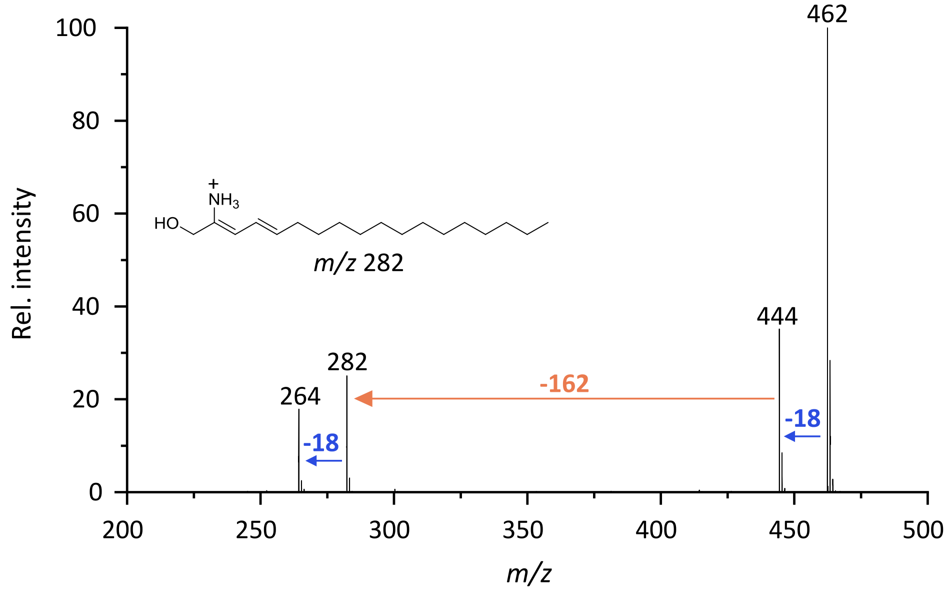

Fig. 18: Exemplary tandem MS spectrum of protonated α-glucosyl sphingosine **3d** obtained by CID (acceleration voltage = 20 V). The three main fragments result from water elimination (-18) and from cleavage of the glycosidic bond yielding dehydrated sphingosine (m/z 282, possible structure shown).

Cold-ion gas phase IR spectra of the protonated monoglycosyl sphingosines **3a-d** were recorded in the region from 900 cm^{-1} to 1800 cm^{-1} while cooling the ion trap (Fig. 19). The isomers are unambiguously distinguishable based on the IR spectra, which are very similar to the corresponding spectra of protonated monoglycosyl phytosphingosines (see Fig. 12). The fingerprint region (1000–1150 cm^{-1}) is characteristic for both the monosaccharide and the anomeric configuration, whereas no distinct absorption bands are present at higher wavenumbers except for the weak NH_3^+ bending vibrations (1400–1500 cm^{-1}) of the protonated primary amine.

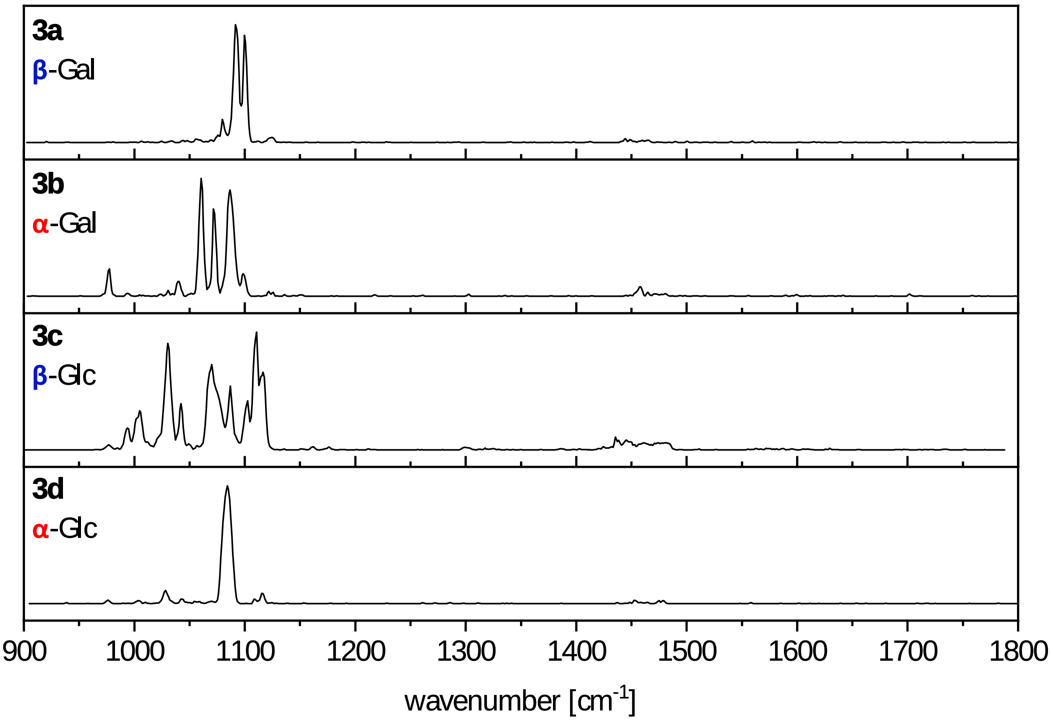

Fig. 19: Stacked IR spectra of protonated α- and β-galactosyl and glucosyl sphingosines (**3a-d**) in the spectral region from 900 cm^{-1} to 1800 cm^{-1}. The spectra were recorded while cooling the trap (-190 °C).

The absorption bands in the fingerprint region are almost identical to the absorptions of the corresponding monoglycosyl phytosphingosines. The absorption frequencies of the most intense, characteristic bands of each combination of monosaccharide and anomeric configuration are independent of the nature of the sphingoid base (Fig. 20); however, slight differences exist on the level of relative intensities. Furthermore, some minor absorption bands are not present in the spectra of both phytosphingosines and sphingosines. For example, the minor absorption next to the main absorption band in the spectrum of α-Glc phytosphingosine (**1d**) is absent in the spectrum of the sphingosine analogue **3d** (see Fig. 20d). Comparing the fingerprint regions of monoglycosyl phytosphingosines and sphingosines leads to the conclusion that the absorption pattern in that region is

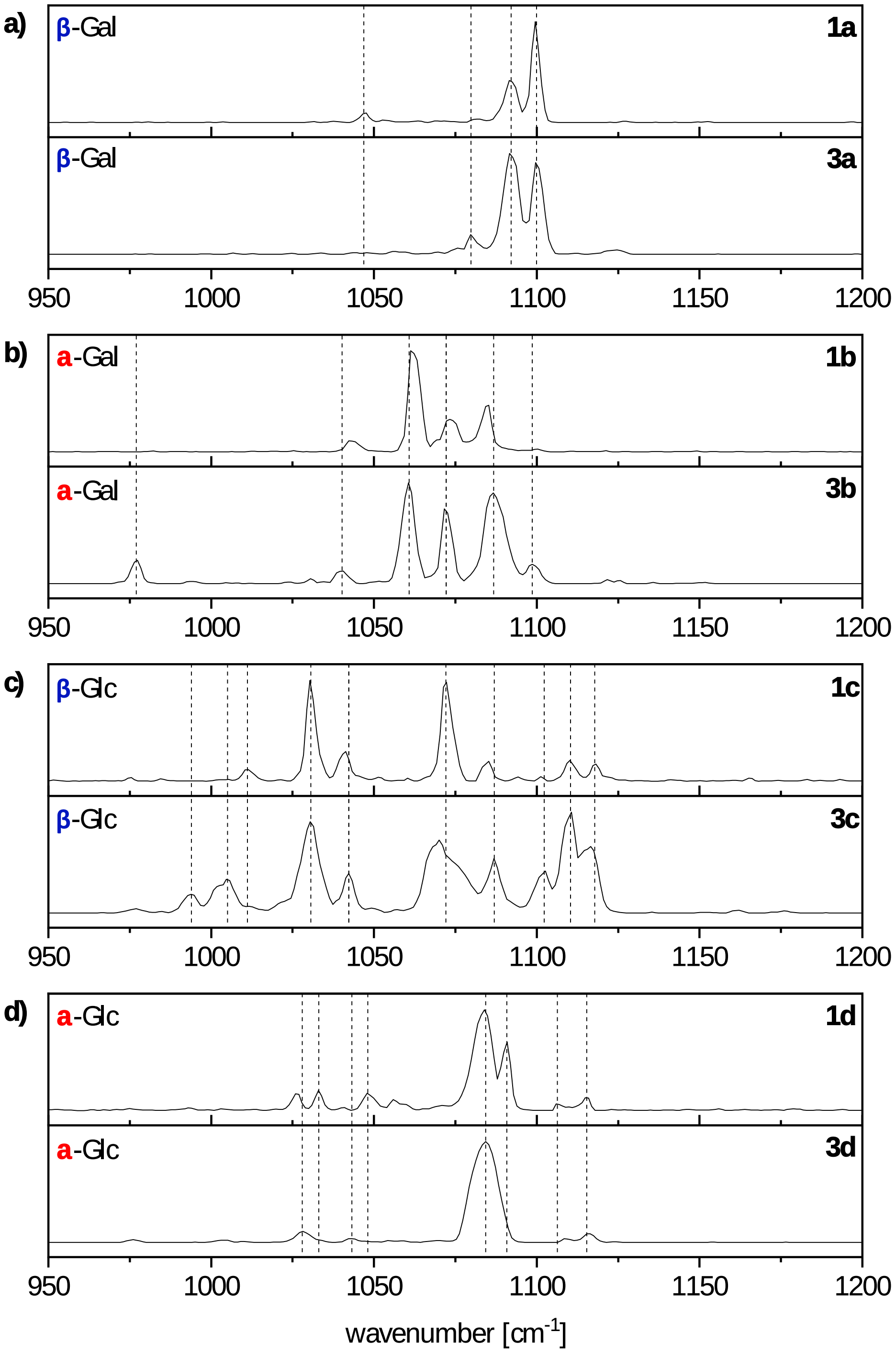

Fig. 20: Comparison of the fingerprint regions in the IR spectra of the protonated monoglycosyl phytosphingosines **1a-d** and monoglycosyl sphingosines **3a-d** measured with a cold trap (-190 °C). The positions of the main absorption bands are determined by the monosaccharide headgroup and its fixed anomeric configuration, which are either β-Gal (a), α-Gal (b), β-Glc (c) or α-Glc (d).

characteristic of the monosaccharide and its anomeric configuration but not significantly changed by a minor structural variation in the sphingoid base. Because the conformation of the monosaccharide is apparently not altered significantly depending on the sphingoid base, the different ion mobilities of monoglycosyl phytosphingosines compared to the sphingosine analogues are likely to arise from different folding of the lipid chain upon the introduction of a double bond. Folding of the sphingoid base affects the overall ion shape and ion mobility but only marginally influences the monosaccharide conformation and thus the monosaccharide-specific vibrations.

The influence of the sphingoid base on the spectral region between 1400 cm^{-1} and 1500 cm^{-1} was investigated by recording IR spectra of protonated monoglycosyl sphingosines without additional cooling of the trap. According to the results previously obtained for the monoglycosyl phytosphingosines, an increase of intensity of the NH_3^+ bending vibrations compared to the spectra recorded with a cold trap was expected (see Fig. 14). The increased temperature in the ion trap caused a slight broadening of absorption bands in the IR spectra of the monoglycosyl sphingosines, which are still well-resolved; however, contrary to the monoglycosyl phytosphingosines, the intensity of the NH_3^+ bending vibrations did not increase with increasing temperature (Fig. 21a). This observation could be explained by the population of different conformations in the trap depending on the sphingoid base. In monoglycosyl sphingosines, conformers in which the NH_3^+ umbrella mode is suppressed by some intramolecular interaction might be energetically favoured, whereas the phytosphingosine analogues adopt conformations in which the NH_3^+ group can vibrate freely. To increase the intensity of the vibrational bands, the region between 1400 cm^{-1} and 1500 cm^{-1} was scanned with a higher laser focus. Unlike the N−H bending vibrations of the monoglycosyl phytosphingosines, which yield well-defined bands with a single maximum, the monoglycosyl sphingosines exhibit split and relatively broad bands. The global position of the NH_3^+ bending vibrations depends on the anomeric configuration; the absorption bands of the β-isomers are centered around 1450 cm^{-1} whereas the center of the absorption bands is located around 1470 cm^{-1} for α-isomers. This anomer-dependent shift of the N−H bending frequency is in perfect accord with the observations made for the corresponding monoglycosyl phytosphingosines (Fig. 21b).

In a study by Poad *et al.*, an intramolecular charge-olefin interaction between the NH_3^+ group and the C=C double bond of 1-deoxysphingosine was predicted (see Section 4.2.3).[7] A similar interaction could take place in monoglycosyl sphingosines, which might lead to a variety of coexisting conformers with different geometries of the sphingoid base and different absorption maxima. The width of the absorption bands could also be a result of the large conformational flexibility of the sphingoid base forming an equilibrium between open lipid chains and lipid chains that are closed into a ring by the charge-olefin interaction. These speculations still need to be confirmed by computational modelling.

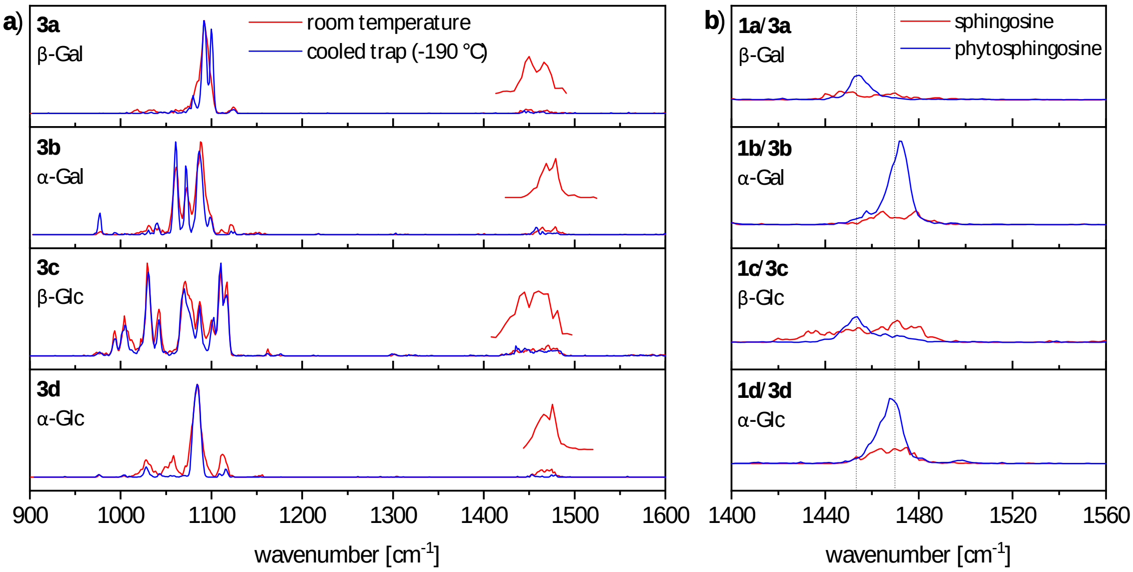

Fig. 21: a) Stacked IR spectra of protonated monoglycosyl sphingosines (**3a-d**) in the spectral region from 900 cm^{-1} to 1600 cm^{-1} recorded with a cold trap (blue traces) or without cooling (red traces). The insets measured with an increased laser focus reveal the splitting of absorption bands and the different absorption frequencies of α- and β-isomers. b) Comparison of NH_3^+ vibrational bands of monoglycosyl phytosphingosines and sphingosines measured without cooling the trap. The anomer-dependent absorption frequencies of sphingosines and phytosphingosines coincide.

In conclusion, the exchange of phytosphingosine by sphingosine has no significant influence on the gas phase IR spectra measured with a cold trap. The fingerprint region remains diagnostic for the monosaccharide and the configuration of the anomeric carbon. Because sphingosine bears a C=C double bond, which is not present in phytosphingosine, it is possible that the protonated amine coordinates to the double bond (see Ref. [7]). Such a charge-olefin interaction may explain the predominance of conformers that do not yield as strong vibrational bands from the NH_3^+ bending vibrations as the conformers of phytosphingosine captured in the trap at room temperature. In sum, the IMS and IR data suggest that the structural difference between sphingosine and phytosphingosine mainly affects the geometry of the lipid chain, whereas the three-dimensional structure of the monosaccharide remains largely unaffected. The monosaccharide conformation is altered only if the sphingoid base is exchanged by a significantly different sphingolipid such as a ceramide (see Fig. 1).

4.2.2 Glycoglycerolipids

The study was extended from GSLs to glycoglycerolipids, a fundamentally different class of glycolipids, to probe the impact of the lipid core structure on the gas phase conformation. A pair of anomeric galactosylglycerolipids (**4a**/**b**) was investigated using the same techniques as employed for the GSLs. Contrary to the GSLs bearing a sphingoid base that is readily protonated, the glycoglycerolipids **4a**/**b** exclusively formed adducts with metal cations. The CCSs of $[M+Na]^+$ and $[M+Ag]^+$ ions were determined by DT-IM-MS (Tab. 5). In accord with the observations made for the GSLs, the CCSs of sodium adducts are larger than the CCSs of the corresponding silver adducts. Both sodium and silver adducts of the α-isomer exhibit slightly shorter drift times than the β-isomer (Fig. 22), but the difference between the CCSs (~ 1 %) is not sufficient for the distinction of the anomers **4a** and **4b** in a mixture. Nevertheless, the results are consistent with the tendency to smaller CCSs for α- than for β-isomers of the monoglycosyl phytosphingosines **1a-d** and **2a**/**b**.

Tab. 5: CCSs of $[M+Na]^+$ and $[M+Ag]^+$ ions of the galactosylglycerolipids **4a**/**b** measured by DT-IM-MS in helium. The $^{DT}CCS_{He}$ values are given in Å^2 (± 1 Å^2).

Sample	$[M+Na]^+$	$[M+Ag]^+$
4a (β-Gal)	210	204
4b (α-Gal)	207	202

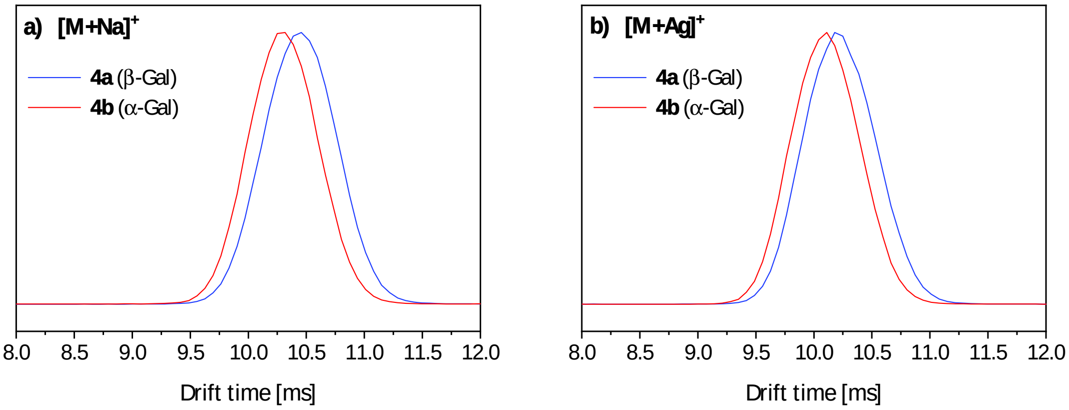

Fig. 22: Drift peaks of $[M+Na]^+$ ions (a) and $[M+Ag]^+$ ions (b) of the anomeric galactosylglycerolipids **4a**/**b**. In both cases, the drift time of the α-anomer is slightly reduced compared to the β-anomer. The drift times were recorded at a constant voltage (IMS Bias = 50 V) and temperature (28.0 ± 0.5 °C).

Cold-ion gas phase IR spectra of sodium adducts were recorded in the spectral range from 900 cm^{-1} to 1800 cm^{-1} while cooling the ion trap (Fig. 23). The spectra display not only the characteristic bands from C−O and C−C stretching vibrations of the sugar ring, which are typically located at wavenumbers below 1250 cm^{-1},[62] but also several absorption bands in the region between 1250 cm^{-1} and 1500 cm^{-1}. These bands could be derived from C−H bending vibrations and C−O stretching vibrations of the esters. The C=O stretching vibrations of the fatty acid esters yield additional bands above 1700 cm^{-1}. The broad band of the C=O stretching vibration in the spectrum of **4a** indicates the presence of more than one conformer or slightly different absorption maxima of the two carbonyl groups merging into one broad band. When superimposing the IR spectra of the anomeric galactosylglycerolipids **4a** and **4b**, most of the bands overlap at least partly. As a consequence, the anomers cannot be easily distinguished by scanning the spectral region between 1000 cm^{-1} and 1150 cm^{-1} as in the case of the GSLs. The assignment is more reliable based on vibrations in the wavenumber range from 1000 cm^{-1} to 1500 cm^{-1}.

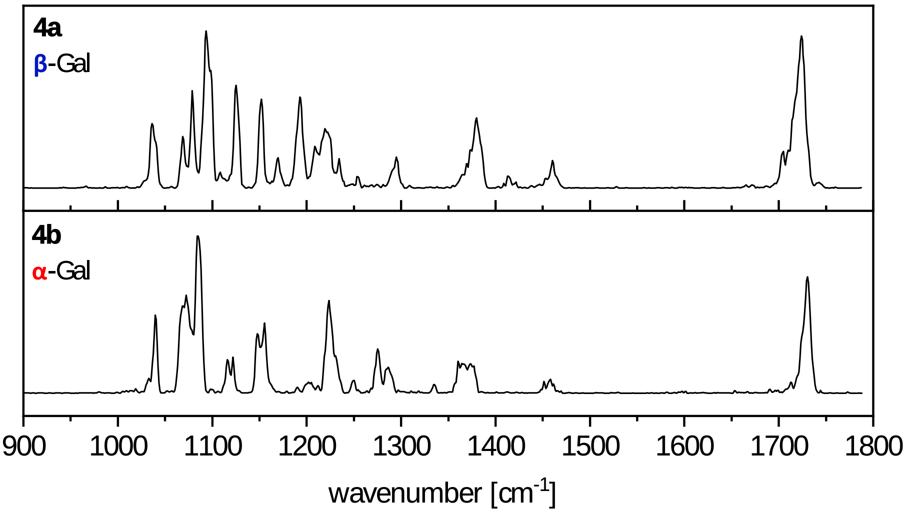

Fig. 23: Stacked IR spectra of sodiated α- and β-galactosylglycerolipids (**4a**/**b**) in the spectral region from 900 cm^{-1} to 1800 cm^{-1}. The spectra were recorded while cooling the ion trap (-190 °C).

When comparing the spectra of the galactosylglycerolipids with the spectra of different GSLs bearing a Gal headgroup such as galactosyl phytosphingosines (**1a**/**b**), galactosyl sphingosines (**3a**/**b**) or GalCer, it becomes evident that the exchange of the sphingoid base by glycerol significantly alters the spectrum (Fig. 24). In the spectra of the galactosylglycerolipids **4a**/**b**, the fingerprint region is not separated from the rest of the spectrum. Multiple absorption bands are present above the upper boundary (1150 cm^{-1}) limiting the fingerprint region of the galactosyl sphingolipids. None of the investigated GSLs yielded strong absorption bands in the region between 1150 cm^{-1} and 1500 cm^{-1}, which are unique for the diacylglycerol backbone. The multitude of absorption bands is not a result of the larger size of the galactosylglycerolipids compared to the monoglycosyl phytosphingosines and sphingosines; α- and β-GalCer also contain two lipid chains but the ceramide influences mainly the spectral region above 1500 cm^{-1} dominated by the amide I and II vibrations, whereas the fingerprint region is still separated from the rest of the spectrum.

In conclusion, the glycoglycerolipids yield fundamentally different IR spectra than the GSLs investigated so far. The spectra of the GSLs display separate fingerprint regions, and different lipid backbones such as phytosphingosine, sphingosine and ceramide mainly

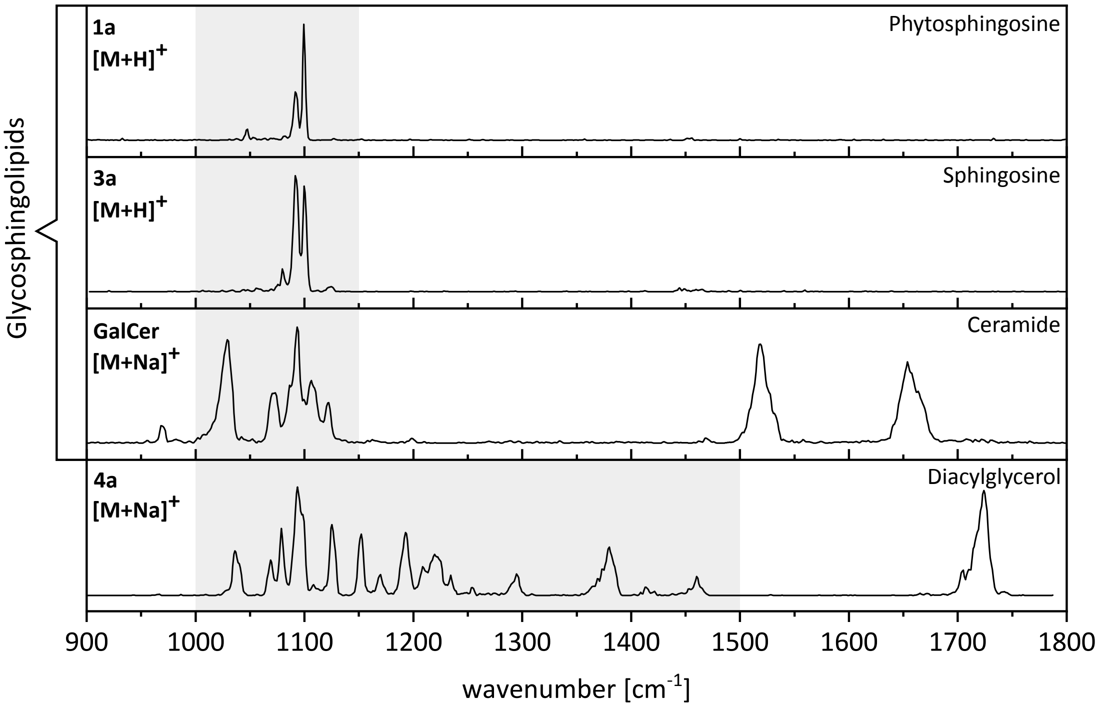

Fig. 24: Stacked IR spectra of β-galactosylglycolipids bearing different lipid residues in the spectral region from 900 cm^{-1} to 1800 cm^{-1}. The GSLs carry either phytosphingosine (**1a**), sphingosine (**3a**) or a ceramide and exhibit well-defined fingerprints in the region between 1000 cm^{-1} and 1150 cm^{-1}. The galactosylglycerolipid (**4a**) yields a significantly different absorption pattern extending up to 1500 cm^{-1}.

influence the spectral region above 1400 cm^{-1}. On the contrary, the defined boundaries of the fingerprint region vanish upon introduction of a glycerol backbone, and several absorption bands appear that seamlessly join the fingerprint region and extend up to 1500 cm^{-1}. The origin of the multiple absorption bands cannot be elucidated without quantum chemical calculations. It is possible that some vibrations are C−O stretching vibrations of the ester groups, which are absent in glycosphingolipids. Some C−H bending vibrations may also be present but too weak to be seen in the spectra of the GSLs.

4.2.3 1-Deoxysphingolipids

1-Deoxysphingolipids were used as model structures to probe the effect of double bond positions and configurations in sphingoid bases on their gas phase conformations. In a previous study, Poad *et al.* predicted an intramolecular charge-olefin interaction between the NH_3^+ group and the double bond of the protonated species.[7] Depending on the double bond position, different geometries of the interaction are expected. 1-Deoxysphingolipids are thus well-suited to test the potential of gas phase IR spectroscopy to distinguish lipid double bond isomers because the N−H bending vibration of the protonated amine can be easily monitored to deduce structural information on the C=C double bond.

The investigated samples **7a-e** are regio- and stereoisomers of 1-deoxysphingosine bearing double bonds at different positions (C 8, 12, 13 or 14) and with different configurations (14*E* or 14*Z*). 1-Deoxysphinganine (**6**) was included as a reference sample in which charge-olefin interactions cannot take place due to the absence of double bonds. The double bond regio- and stereoisomers were investigated using DT-IM-MS and cryogenic gas phase IR spectroscopy. IM-MS measurements of the protonated species showed that all samples readily eliminate water to form $[M+H-H_2O]^+$ fragments. The CCSs of $[M+H]^+$ and $[M+H-H_2O]^+$ ions are listed below (Tab. 6).

Tab. 6: CCSs of $[M+H]^+$ and $[M+H-H_2O]^+$ ions of 1-deoxysphinganine (**6**) and of 1-deoxysphingosine isomers (**7a-e**) measured by DT-IM-MS in helium. The $^{DT}CCS_{He}$ values are given in Å^2 (± 1 Å^2).

Sample	$[M+H]^+$	$[M+H-H_2O]^+$
6	120	119
7a (8*E*)	117	116
7b (12*E*)	117	117
7c (13*E*)	116	115
7d (14*E*)	117	116
7e (14*Z*)	115	114

The CCSs of $[M+H]^+$ ions are identical for all double bond regioisomers **7a-d**. As expected, the CCSs of 1-deoxysphinganine ions are about 2 % larger than the CCSs of the 1-deoxysphingosine isomers. The decrease of CCSs upon introduction of a double bond into the sphingoid base was already observed for the exchange of saturated phytosphingosine by unsaturated sphingosine (see Section 4.2.1) and is confirmed in the literature for other lipid classes.[7,49] The CCS of the protonated 14*Z* stereoisomer **7e** is about 2 Å^2 smaller than the CCSs of *E* double bond isomers. This observation is consistent with other IMS studies on lipid double bond stereoisomers, which revealed a more compact shape of *Z* isomers compared to the corresponding *E* isomers.[18,49] The separation of the protonated species into three groups, namely 1-deoxysphinganine, the *E* double bond regioisomers and the 14*Z* double bond stereoisomer, can be directly seen from the drift peaks (Fig. 25a). The drift times of the double bond regioisomers **7a-d** are almost identical, whereas the drift peak of the 14*Z* isomer **7e** is slightly shifted to shorter drift times and the drift time of 1-deoxysphinganine **6** is distinctly longer. The 12*E* and 13*E* isomers can be distinguished better as $[M+H-H_2O]^+$ ions (Fig. 25b). The CCS of the $[M+H-H_2O]^+$ ion of the 12*E* isomer is identical with the CCS of the $[M+H]^+$ ion, whereas the smallest CCSs were found for the 13*E* isomer. The CCSs of the 8*E* and 14*E* isomers are intermediate.

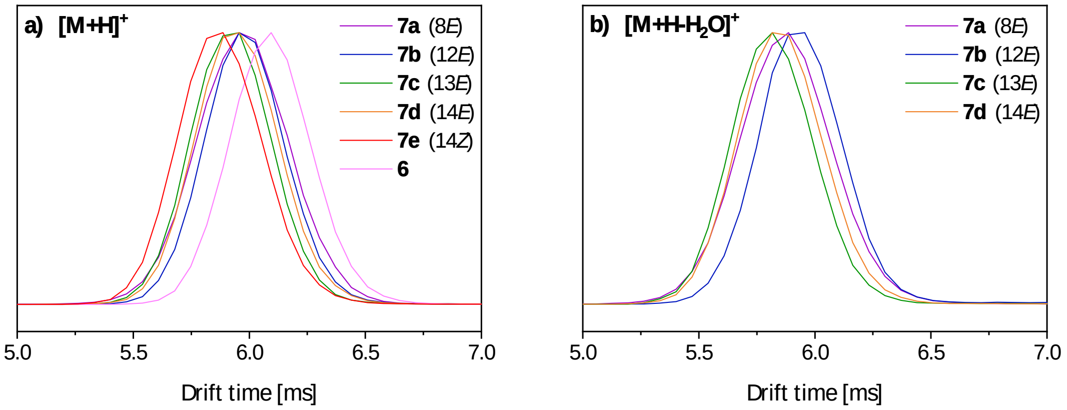

Fig. 25: Drift peaks of $[M+H]^+$ ions (a) and $[M+H–H_2O]^+$ ions (b) of 1-deoxysphingolipids. The drift times of the $[M+H]^+$ ions depend on the presence of a double bond and its configuration. The double bond regioisomers 12*E* and 13*E* can be distinguished based on the drift times of the $[M+H–H_2O]^+$ ions. The drift times were recorded at the same voltage (IMS Bias = 50 V) and temperature (27.0 ± 0.5°C).

The DT-IM-MS measurements were repeated using a home-built linear drift tube instrument with a drift tube length of about 80 cm.[1] Technical details can be found elsewhere.[53] Owing to the longer drift region, the instrument provides a higher resolution than the modified Synapt instrument. The additional IMS data were acquired to test if the separation of double bond regioisomers could be increased and to confirm the reproducibility of the ion mobility trends on different instruments. The arrival time distributions were measured at a fixed drift voltage. The protonated double bond regioisomers could be separated based on their drift times in the following order: $13E < 8E = 14E < 12E$ (Fig. 26a). The 13*E* isomer yielded a particularly broad drift peak indicating the presence of multiple conformers. The drift peaks of the 8*E* and 14*E* isomers could not be separated; however, the drift peak shape of the 8*E* isomer is distinct and implies the coexistence of at least two populations with significantly different drift times. The drift peak of the characteristic $[M+H–H_2O]^+$ fragment of the 8*E* isomer exhibits the same shape, which is an indication that the peak shape is not just resulting from an impurity at the same m/z as the $[M+H]^+$ ion (Fig. 26c). The IMS measurements on the Synapt instrument did not reveal the presence of more than one conformer, which could be attributed to its harsher source conditions that can alter the distribution of conformers. In accord with the results from the Synapt instrument, the separation of the 12*E* and 13*E* isomers was slightly increased for the $[M+H–H_2O]^+$ ions, which yielded in general broader drift peaks than the protonated species. The separation of the drift peaks of the double bond stereoisomers could equally be increased by the higher resolution (Fig. 26b). The pure 14*E* and 14*Z* isomers are clearly distinguishable; still, the separate drift peaks are not resolved in a 1:1 mixture.

---

[1] The instrument was operated by Maike Lettow.

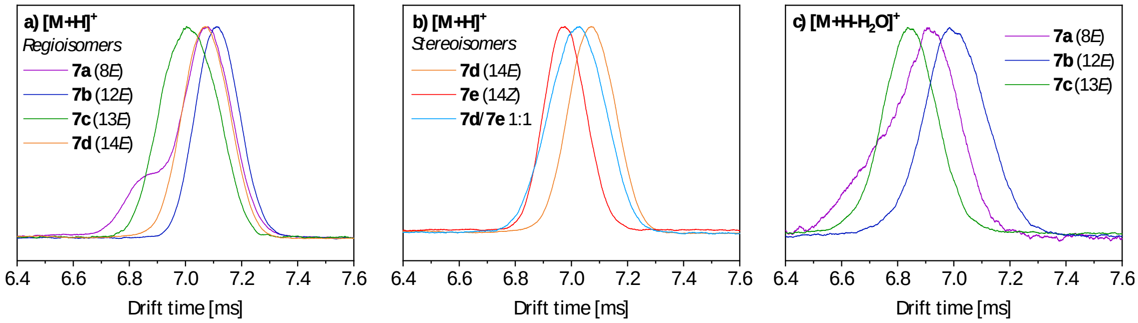

Fig. 26: Drift peaks of $[M+H]^+$ ions and $[M+H–H_2O]^+$ ions of 1-deoxysphingolipids measured by high-resolution DT-IM-MS in helium. The $[M+H]^+$ ions of the double bond regioisomers (a) and of the pure stereoisomers (b) are distinguishable but not resolved in a mixture. The drift peaks of the 12*E* and 13*E* isomers are slightly better separated as $[M+H–H_2O]^+$ ions (c).

The 1-deoxysphingosine double bond regioisomers were previously investigated by Poad *et al.* using differential-mobility spectrometry (DMS). In DMS, ions are separated in space while they travel in an electric field between two electrodes on a trajectory that is modified by a gas flowing parallel to the electrodes.[46] Larger ions are more deflected by collisions with the gas than smaller ions and thus require a larger compensation voltage to reach the slit in the second electrode. The protonated double bond regioisomers of 1-deoxysphingosine could be separated by DMS and the reported compensation voltages increase in the following order: $14E < 8E < 13E < 12E$. The order correlates well with the drift times found by DT-IMS except for the 13*E* isomer, which yielded the shortest drift time. The DMS data also showed that the 14*E* and 8*E* isomers, which could not be separated by DT-IMS, exhibit very similar ion mobilities. In conclusion, different high-resolution IMS techniques can be used to distinguish the double bond regio- and stereoisomers **7a-e**; however, the 8*E* and 14*E* isomers could not be distinguished by DT-IMS and the analysis of mixtures was not possible with the available resolution. The regioisomers **7a-d** could not be separated using the modified Synapt instrument, which provides only about half the resolution offered by the home-built ion mobility spectrometer. The $^{DT}CCS_{N_2}$ values reported by Poad *et al.* are also identical for all regioisomers.

Gas phase IR spectra of the protonated 12*E* and 14*E* regioisomers were recorded in the spectral range from 900 cm^{-1} to 1800 cm^{-1} while cooling the ion trap (Fig. 27). The strongest absorption bands are located between 1400 cm^{-1} and 1500 cm^{-1} and attributed to N–H bending vibrations of the NH_3^+ group. The absorption frequencies are clearly shifted depending on the double bond position: the absorption maximum of the 12*E* isomer (**7b**) is located around 1430 cm^{-1}, whereas the absorption maximum is shifted to 1450 cm^{-1} for the 14*E* isomer (**7d**). The shift of 20 cm^{-1} is considerable and reproducible. Furthermore, the spectra suggest the presence of multiple conformers of both regioisomers. The absorption bands of the N–H bending vibration are relatively broad and cover 30–40 cm^{-1}, which

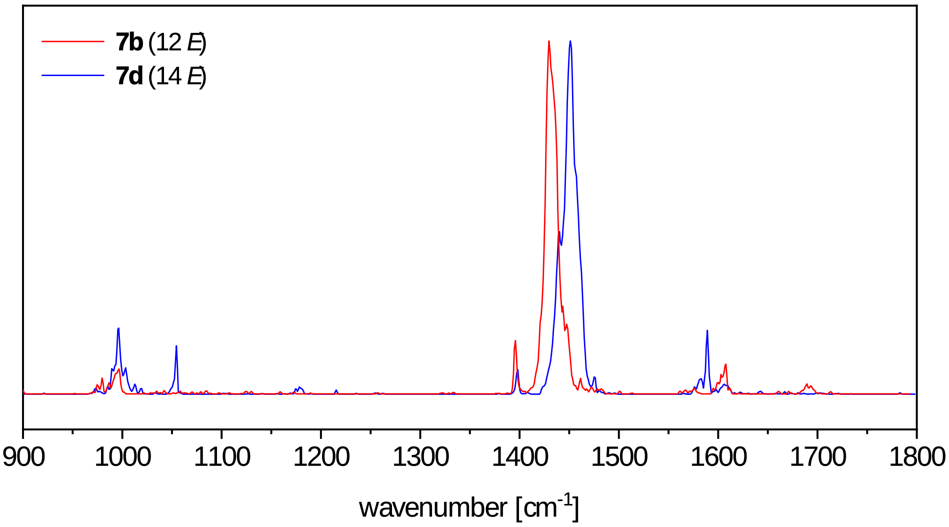

Fig. 27: Superimposed gas phase IR spectra of 12*E* and 14*E* double bond isomers of 1-deoxysphingosine in the region from 900 cm^{-1} to 1800 cm^{-1}. The most intense absorption bands are attributed to N—H bending vibrations and shifted depending on the double bond position. The spectra were recorded while cooling the ion trap (-190 °C).

is an indication for a large conformational flexibility of the lipid chains in the gas phase. The coexistence of different conformers with similar free energies and slightly different absorption frequencies causes broad absorption bands, which reflect an equilibrium of different geometries adopted by the lipid chain. Some conformers might be present in both regioisomers because the absorption bands overlap partially; however, the overall distribution of conformers changes with the double bond position.

Apart from the intense NH_3^+ umbrella vibration, the spectra exhibit several less intense absorption bands in the range of C—O stretching vibrations below 1100 cm^{-1}. The absorption band at 1400 cm^{-1} in both spectra might result from C—O—H bending modes.[64] The absorptions around 1600 cm^{-1}, which are shifted according to the double bond positions, are likely to result from NH_3^+ scissoring modes.[64] The main information can, however, be extracted by scanning only the short spectral range from 1400 cm^{-1} to 1500 cm^{-1} dominated by the NH_3^+ umbrella motion. For that reason, IR spectra of the other samples were recorded only in the range from 1350 cm^{-1} to 1550 cm^{-1} (Fig. 28). Each sample yielded diagnostic absorption bands, which are clearly distinguishable from the other samples with the exception of the 13*E* and 14*Z* isomers exhibiting quasi-identical spectra. This coincidence could result from similar geometries of the lipid chains, which would be supported by the similar ion mobilities, or from different geometries in which the N—H bending occurs at the same wavenumber by chance. Apart from the different absorption maxima, the absorption band structures are also very characteristic for each isomer. Multiple conformers seem to

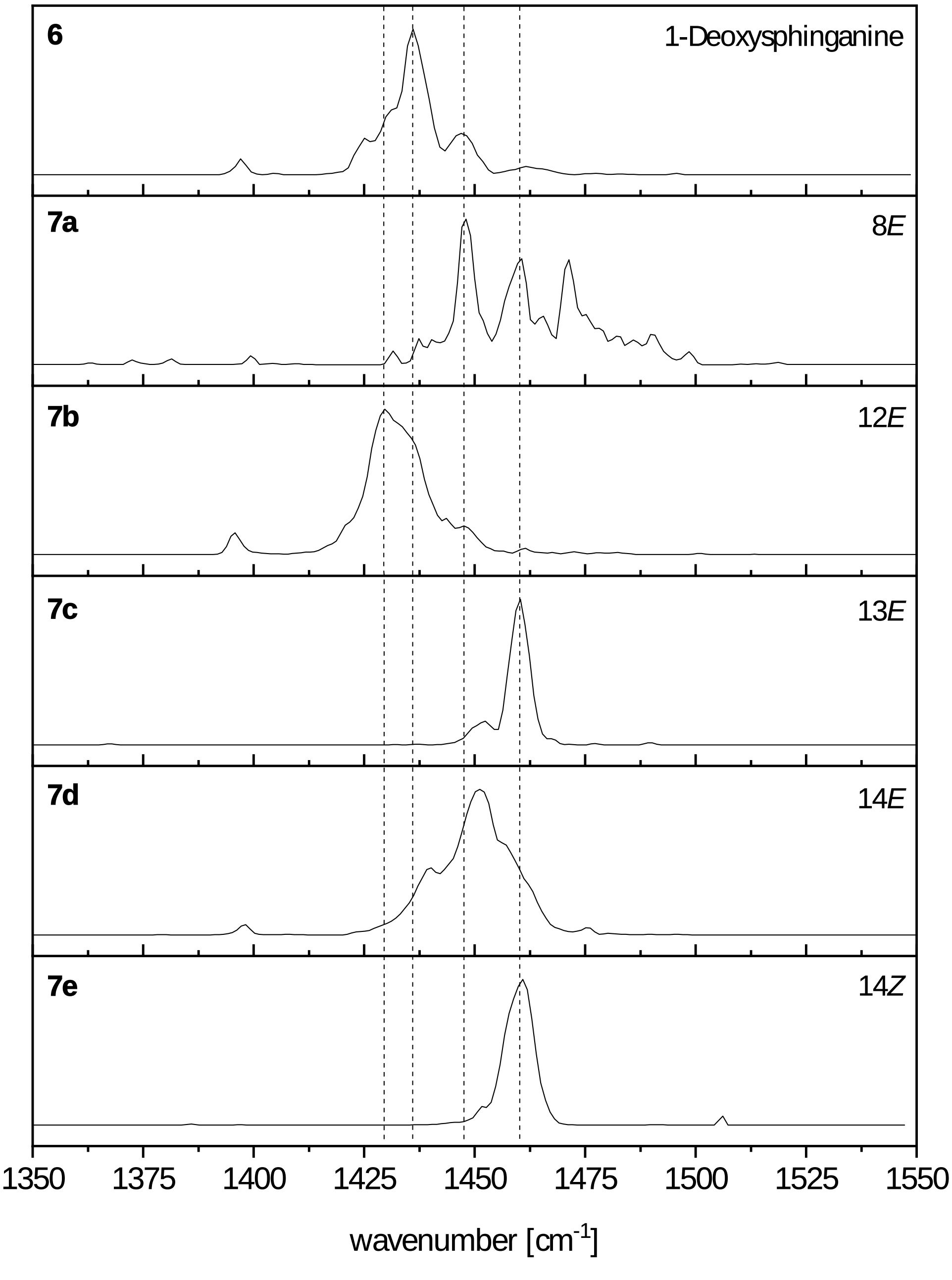

Fig. 28: Stacked IR spectra of protonated 1-deoxysphinganine **6** and of protonated double bond isomers of 1-deoxysphingosine (**7a**-**e**) in the region from 1350 cm^{-1} to 1550 cm^{-1}. The positions and band structures of the N—H bending vibrations are characteristic of the double bond position and configuration. Most of the spectra have several absorption maxima in common, which are indicated by dashed horizontal lines. The spectra were recorded while cooling the ion trap (-190 °C).

be present in most of the spectra, which exhibit multiple absorption maxima and broad absorption bands. The conformational flexibility is particularly obvious in the case of the 8*E* isomer, which absorbs in a broad range covering more than $50\,\text{cm}^{-1}$ and displays distinct absorption maxima. This observation is in accord with the IMS data, which revealed the presence of at least two significantly different populations in the gas phase; nevertheless, the conformer distributions are not necessarily comparable between different instruments owing to different source conditions and temperatures. In particular, the low temperature in the ion trap can lead to depopulation of higher-energy conformers observed under the gentle conditions in the drift tube at room temperature.

The conformational flexibility supports the assumption of intramolecular charge-olefin interactions resulting in an equilibrium of open-chain and closed-ring lipid structures; however, the existence of that interaction cannot be directly proven by IR spectroscopy. 1-Deoxysphinganine (**6**) exhibits several absorption maxima, which indicate that the lipid chain adopts multiple conformations also in the absence of charge-olefin interactions. Some absorption maxima of the reference sample are also present in the spectra of the double bond isomers, which hints to the presence of a considerable amount of open-chain conformers; nevertheless, most of the double bond isomers exhibit absorption bands that are not present in the reference spectrum of 1-deoxysphinganine and that could result from closed-ring conformers. Molecular dynamics simulations performed by Poad *et al.* did not identify a preference for charge-olefin interactions in the protonated 8*E* isomer, contrary to the other regioisomers that are assumed to favour this intramolecular interaction.

The data show that cryogenic gas phase IR spectroscopy is a sensitive technique to identify double bond positions and configurations in well-defined systems such as 1-deoxysphingolipids. The double bond is not directly monitored but the different molecular conformations induced by the double bond are indirectly probed *via* vibrations of neighbouring functional groups such as the NH_3^+ group in this case.

5. Conclusions and Outlook

This work provides the first study employing cryogenic gas phase IR spectroscopy to systematically investigate glycolipid structures and to unravel conformational differences in isomeric species that are indistinguishable by standard (tandem-)MS or IM-MS. Using an exemplary model set of GSLs consisting of a sphingoid base and a monosaccharide headgroup, it was demonstrated that different monosaccharides and anomeric configurations can be unambiguously distinguished by scanning a relatively short spectral range (1000–1150 cm^{-1}). This region is referred to as the *fingerprint region*, which is characterized by highly diagnostic and well-resolved bands from coupled C−O and C−C stretching vibrations of the glycan. The effect of the glycan size on the resolution of the IR fingerprint was probed by comparing monosaccharide and trisaccharide headgroups. It was shown that the absorption bands in the fingerprint region of a trisaccharide are still well-resolved but no longer baseline-separated. Furthermore, the influence of different lipid moieties was probed by comparing IR spectra of sphingosine, phytosphingosine, ceramide and diacylglycerol moieties attached to monosaccharide headgroups. The fingerprint regions in the IR spectra of monoglycosyl sphingosines and monoglycosyl phytosphingosines are almost identical, which leads to the conclusion that the three-dimensional structure of the monosaccharide is not significantly affected by the exchange of the sphingoid base. However, the sphingoid base influences the relative intensity of the N−H bending vibration located between 1400 cm^{-1} and 1500 cm^{-1}. Hence, the exchange of the sphingoid base probably induces different foldings of the lipid chain. The frequency of the N−H bending vibration was further found to be indicative for the anomeric configuration ($\sim$ 1450 cm^{-1} for β-Glc/Gal and $\sim$ 1470 cm^{-1} for α-Glc/Gal). The study was completed by investigating a pair of anomeric galactosylglycerolipids bearing a fundamentally different lipid moiety. The resulting IR spectra differ significantly from the spectra of the corresponding galactosylsphingolipids. In particular, several absorption bands appear beyond the fingerprint region between 1150 cm^{-1} and 1500 cm^{-1}. On the contrary, the IR spectra of all investigated GSLs exhibit fingerprint regions that are well-separated from the rest of the spectrum, whereas the sphingolipid mainly influences the spectral range above 1400 cm^{-1}. The study was accompanied by DT-IM-MS measurements and determination of CCSs. In most cases, isomeric glycolipids could not be distinguished, with the exception of α- and β-monoglycosyl phytosphingosines that are separable as silver adducts.

The information content of the high-resolution IR spectra can only be fully exploited by comparisons with quantum chemical calculations to determine the three-dimensional glycolipid structures. Density functional theory calculations thus have to be performed. However, recent calculations have shown that the coupled vibrations in the fingerprint region cannot be accurately modeled, which was attributed to possible anharmonicities.

This lack of accuracy could be a major hurdle for structure determination of glycolipids that do not display characteristic absorption bands beyond the fingerprint region. A major interest of studying isomeric glycolipids consists in the reliable characterization of isomeric mixtures in biological samples including the detection of low-abundant but biologically active species. The detection of minor impurities would also be highly interesting for quality control in stereoselective glycolipid synthesis. In this respect, the possibility to differentiate isomers in a mixture and to quantify their ratio based on IR spectroscopy will be explored in future experiments. Mixtures of biologically relevant, synthetically pure α- and β-glycosylceramides will be prepared in different ratios and measured by gas phase IR spectroscopy to determine the limit of sensitivity of the technique. Finally, IR spectra of a biological mixture of glycolipid anomers will be recorded and ideally, the α:β-ratio can be estimated semi-quantitatively with the help of the spectra from synthetic standards.

The second part of the study was dedicated to the investigation of 1-deoxysphingosine double bond regio- and stereoisomers. A previous study suggested the existence of intramolecular charge-olefin interactions between the protonated primary amine and the C=C double bond, which was expected to affect the geometry of the lipid chain and thus the ion mobility and the N−H bending vibrations. The double bond isomers were distinguishable by high-resolution DT-IM-MS but could not be resolved in a mixture. The gas phase IR spectra, however, are very diagnostic for the double bond position and configuration owing to the NH_3^+ umbrella modes, which are shifted according to the molecular geometry. The importance of charge-olefin interactions was not directly proven by this study but the presence of several low-energy conformers was confirmed by multiple or broad absorption bands. Among these conformers, open-chain and closed-ring structures may exist. Overall, the results constitute a proof of principle that double bond isomers can be distinguished by IR spectroscopy, provided that the vibration of a diagnostic functional group is affected by the double bond position and configuration.

In the near future, the set of 1-deoxysphingolipids will be complemented with regioisomers bearing the double bond closer to the NH_3^+ group (4*E* and 5*E*). The proximity of the double bond to the protonated amine is expected to have an influence on the shape of the molecular ions and should affect the IR spectra. According to Poad *et al.*, the NH_3^+ group is positioned directly above the C=C double bond if the double bond is located at the end of the chain (12*E*, 13*E* and 14*E*), whereas it must be placed off-axis in the 4*E* and 5*E* isomers.[7] The underlying gas phase structures will be searched by quantum chemical calculations and correlated with the observed shifts of absorption bands. Building on the knowledge gained on 1-deoxysphingosine double bond isomers, other biologically relevant sphingolipids such as for example isomeric 1-deoxyphytosphingosine and ω-hydroxy-1-deoxysphinganine will be investigated by gas phase IR spectroscopy.

References

[1] T. Yamashita, R. Wada, T. Sasaki, C. Deng, U. Bierfreund, K. Sandhoff, R. L. Proia, *Proc. Natl. Acad. Sci. U.S.A.* **1999**, *96*, 9142–9147.

[2] H. Farwanah, T. Kolter, *Metabolites* **2012**, *2*, 134–164.

[3] K. Seino, M. Taniguchi, *Front. Biosci.* **2004**, *9*, 2577–2587.

[4] L. Kain, A. Costanzo, B. Webb, M. Holt, A. Bendelac, P. B. Savage, L. Teyton, *Mol. Immunol.* **2015**, *68*, 94–97.

[5] T. Kawano, J. Cui, Y. Koezuka, I. Toura, Y. Kaneko, K. Motoki, H. Ueno, R. Nakagawa, H. Sato, E. Kondo, H. Koseki, M. Taniguchi, *Science* **1997**, *278*, 1626–1629.

[6] L. Kain, B. Webb, B. L. Anderson, S. Deng, M. Holt, A. Costanzo, M. Zhao, K. Self, A. Teyton, C. Everett, M. Kronenberg, D. M. Zajonc, A. Bendelac, P. B. Savage, L. Teyton, *Immunity* **2014**, *41*, 543–554.

[7] B. L. J. Poad, A. T. Maccarone, H. Yu, T. W. Mitchell, E. M. Saied, C. Arenz, T. Hornemann, J. N. Bull, E. J. Bieske, S. J. Blanksby, *Anal. Chem.* **2018**, *90*, 5343–5351.

[8] F. H. Crick, *Symp. Soc. Exp. Biol.* **1958**, *12*, 138–163.

[9] A. Varki, S. Kornfeld in *Essentials of Glycobiology*, (Eds.: A. Varki, R. D. Cummings, J. D. Esko, P. Stanley, G. W. Hart, M. Aebi, A. G. Darvill, T. Kinoshita, N. H. Packer, J. H. Prestegard, R. L. Schnaar, P. H. Seeberger), Cold Spring Harbor (NY), **2015**, pp. 1–18.

[10] S. Ghosh, J. C. Strum, R. M. Bell, *FASEB J.* **1997**, *11*, 45–50.

[11] R. A. Dwek, *Chem. Rev.* **1996**, *96*, 683–720.

[12] R. S. Haltiwanger, J. B. Lowe, *Annu. Rev. Biochem.* **2004**, *73*, 491–537.

[13] B. Chen, Y. Sun, J. Niu, G. K. Jarugumilli, X. Wu, *Cell Chem. Biol.* **2018**, *25*, 817–831.

[14] H. Jiang, X. Zhang, X. Chen, P. Aramsangtienchai, Z. Tong, H. Lin, *Chem. Rev.* **2018**, *118*, 919–988.

[15] K. Ohtsubo, J. D. Marth, *Cell* **2006**, *126*, 855–867.

[16] M. A. Chester, *Eur. J. Biochem.* **1998**, *257*, 293–298.

[17] R. L. Schnaar, T. Kinoshita in *Essentials of Glycobiology*, (Eds.: A. Varki, R. D. Cummings, J. D. Esko, P. Stanley, G. W. Hart, M. Aebi, A. G. Darvill, T. Kinoshita, N. H. Packer, J. H. Prestegard, R. L. Schnaar, P. H. Seeberger), Cold Spring Harbor Laboratory Press, Cold Spring Harbor (NY), **2015**, pp. 125–135.

[18] R. Wojcik, I. K. Webb, L. Deng, S. V. Garimella, S. A. Prost, Y. M. Ibrahim, E. S. Baker, R. D. Smith, *Int. J. Mol. Sci.* **2017**, *18*, 183.

[19] S. T. Pruett, A. Bushnev, K. Hagedorn, M. Adiga, C. A. Haynes, M. C. Sullards, D. C. Liotta, A. H. Merrill, *J. Lipid Res.* **2008**, *49*, 1621–1639.

[20] A. H. Merrill, *Chem. Rev.* **2011**, *111*, 6387–6422.

[21] K. Hanada, *Biochim. Biophys. Acta* **2003**, *1632*, 16–30.

[22] A. H. Merrill, M. D. Wang, M. Park, M. C. Sullards, *Trends Biochem. Sci.* **2007**, *32*, 457–468.

[23] K. Simons, E. Ikonen, *Nature* **1997**, *387*, 569–572.

[24] D. Hoekstra, O. Maier, J. M. van der Wouden, T. A. Slimane, S. C. D. van Ijzendoorn, *J. Lipid Res.* **2003**, *44*, 869–877.

[25] W. Stoffel, A. Bosio, *Curr. Opin. Neurobiol.* **1997**, *7*, 654–661.

[26] L. K. Ryland, T. E. Fox, X. Liu, T. P. Loughran, M. Kester, *Cancer Biol. Ther.* **2011**, *11*, 138–149.

[27] B. Weiss, W. Stoffel, *Eur. J. Biochem.* **1997**, *249*, 239–247.

[28] A. Penno, M. M. Reilly, H. Houlden, M. Laura, K. Rentsch, V. Niederkofler, E. T. Stoeckli, G. Nicholson, F. Eichler, R. H. Brown, A. von Eckardstein, T. Hornemann, *J. Biol. Chem.* **2010**, *285*, 11178–11187.

[29] R. Steiner, E. M. Saied, A. Othman, C. Arenz, A. T. Maccarone, B. L. Poad, S. J. Blanksby, A. von Eckardstein, T. Hornemann, *J. Lipid Res.* **2016**, *57*, 1194–1203.

[30] I. Alecu, A. Othman, A. Penno, E. M. Saied, C. Arenz, A. von Eckardstein, T. Hornemann, *J. Lipid Res.* **2017**, *58*, 60–71.

[31] J. Mwinyi, A. Bostrom, I. Fehrer, A. Othman, G. Waeber, H. Marti-Soler, P. Vollenweider, P. Marques-Vidal, H. B. Schioth, A. von Eckardstein, T. Hornemann, *PLoS One* **2017**, *12*, e0175776.

[32] J. M. Rini, J. D. Esko in *Essentials of Glycobiology*, (Eds.: rd, A. Varki, R. D. Cummings, J. D. Esko, P. Stanley, G. W. Hart, M. Aebi, A. G. Darvill, T. Kinoshita, N. H. Packer, J. H. Prestegard, R. L. Schnaar, P. H. Seeberger), Cold Spring Harbor (NY), **2015**, pp. 65–75.

[33] M. C. Sullards, Y. Liu, Y. Chen, A. H. Merrill, *Biochim. Biophys. Acta* **2011**, *1811*, 838–853.

[34] T. W. Mitchell, H. Pham, M. C. Thomas, S. J. Blanksby, *J. Chromatogr. B Analyt. Technol. Biomed. Life Sci.* **2009**, *877*, 2722–2735.

[35] I. Meisen, M. Mormann, J. Muthing, *Biochim. Biophys. Acta* **2011**, *1811*, 875–896.

[36] S. N. Jackson, B. Colsch, T. Egan, E. K. Lewis, J. A. Schultz, A. S. Woods, *Analyst* **2011**, *136*, 463–466.

[37] C. E. Randolph, D. J. Foreman, S. J. Blanksby, S. A. McLuckey, *Anal. Chem.* **2019**, *91*, 9032–9040.

[38] M. C. Thomas, T. W. Mitchell, D. G. Harman, J. M. Deeley, J. R. Nealon, S. J. Blanksby, *Anal. Chem.* **2008**, *80*, 303–311.

[39] B. L. Poad, H. T. Pham, M. C. Thomas, J. R. Nealon, J. L. Campbell, T. W. Mitchell, S. J. Blanksby, *J. Am. Soc. Mass Spectrom.* **2010**, *21*, 1989–1999.

[40] J. Hofmann, H. S. Hahm, P. H. Seeberger, K. Pagel, *Nature* **2015**, *526*, 241–244.

[41] T. R. Rizzo, O. V. Boyarkin, *Top. Curr. Chem.* **2015**, *364*, 43–97.

[42] E. Mucha, A. I. González Flórez, M. Marianski, D. A. Thomas, W. Hoffmann, W. B. Struwe, H. S. Hahm, S. Gewinner, W. Schöllkopf, P. H. Seeberger, G. von Helden, K. Pagel, *Angew. Chem. Int. Ed.* **2017**, *56*, 11248–11251.

[43] K. Brandenburg, U. Seydel, *Chem. Phys. Lipids* **1998**, *96*, 23–40.

[44] D. A. Mannock, R. N. A. H. Lewis, R. N. McElhaney, *Chem. Phys. Lipids* **1990**, *55*, 309–321.

[45] V. Gabelica, A. A. Shvartsburg, C. Afonso, P. Barran, J. L. P. Benesch, C. Bleiholder, M. T. Bowers, A. Bilbao, M. F. Bush, J. L. Campbell, I. D. G. Campuzano, T. Causon, B. H. Clowers, C. S. Creaser, E. De Pauw, J. Far, F. Fernandez-Lima, J. C. Fjeldsted, K. Giles, M. Groessl, J. Hogan, C. J., S. Hann, H. I. Kim, R. T. Kurulugama, J. C. May, J. A. McLean, K. Pagel, K. Richardson, M. E. Ridgeway, F. Rosu, F. Sobott, K. Thalassinos, S. J. Valentine, T. Wyttenbach, *Mass Spectrom. Rev.* **2019**, *38*, 291–320.

[46] R. Cumeras, E. Figueras, C. E. Davis, J. I. Baumbach, I. Gracia, *Analyst* **2015**, *140*, 1376–1390.

[47] H. H. Hill, W. F. Siems, R. H. St. Louis, *Anal. Chem.* **1990**, *62*, 1201A–1209A.

[48] J. Hofmann, K. Pagel, *Angew. Chem. Int. Ed.* **2017**, *56*, 8342–8349.

[49] J. E. Kyle, X. Zhang, K. K. Weitz, M. E. Monroe, Y. M. Ibrahim, R. J. Moore, J. Cha, X. Sun, E. S. Lovelace, J. Wagoner, S. J. Polyak, T. O. Metz, S. K. Dey, R. D. Smith, K. E. Burnum-Johnson, E. S. Baker, *Analyst* **2016**, *141*, 1649–1659.

[50] A. M. Rijs, J. Oomens, *Top. Curr. Chem.* **2015**, *364*, 1–42.

[51] J. Oomens, B. G. Sartakov, G. Meijer, G. von Helden, *Int. J. Mass spectrom.* **2006**, *254*, 1–19.

[52] A. I. González Flórez, *Biomolecular Ions in Helium Nanodroplets*, Thesis, Freie Universität Berlin, **2016**.

[53] S. Warnke, *A Gas-Phase Approach to Biomolecular Structure: Combining Ion Mobility-Mass Spectrometry with Spectroscopy*, Thesis, Freie Universität Berlin, **2015**.

[54] M. Brümmer, C. Kaposta, G. Santambrogio, K. R. Asmis, *J. Chem. Phys.* **2003**, *119*, 12700–12703.

[55] S. Goyal, D. L. Schutt, G. Scoles, *Phys. Rev. Lett.* **1992**, *69*, 933–936.

[56] F. Bierau, P. Kupser, G. Meijer, G. von Helden, *Phys. Rev. Lett.* **2010**, *105*, 133402.

[57] J. P. Toennies, A. F. Vilesov, *Angew. Chem. Int. Ed.* **2004**, *43*, 2622–2648.

[58] S. Smolarek, N. B. Brauer, W. J. Buma, M. Drabbels, *J. Am. Chem. Soc.* **2010**, *132*, 14086–14091.

[59] A. I. González Flórez, D. S. Ahn, S. Gewinner, W. Schöllkopf, G. von Helden, *Phys. Chem. Chem. Phys.* **2015**, *17*, 21902–21911.

[60] W. Schöllkopf, S. Gewinner, H. Junkes, A. Paarmann, G. von Helden, H. Bluem, A. M. M. Todd, *Proc. SPIE Int. Soc. Opt.* **2015**, *9512*.

[61] E. M. Saied, T. L. Le, T. Hornemann, C. Arenz, *Bioorg. Med. Chem.* **2018**, *26*, 4047–4057.

[62] E. Mucha, M. Marianski, F. F. Xu, D. A. Thomas, G. Meijer, G. von Helden, P. H. Seeberger, K. Pagel, *Nat. Commun.* **2018**, *9*, 4174.

[63] V. Lepere, K. Le Barbu-Debus, C. Clavaguera, D. Scuderi, G. Piani, A. L. Simon, F. Chirot, L. MacAleese, P. Dugourd, A. Zehnacker, *Phys. Chem. Chem. Phys.* **2016**, *18*, 1807–1817.

[64] J. Seo, W. Hoffmann, S. Malerz, S. Warnke, M. T. Bowers, K. Pagel, G. von Helden, *Int. J. Mass Spectrom.* **2018**, *429*, 115–120.

[65] A. T. Maccarone, J. Duldig, T. W. Mitchell, S. J. Blanksby, E. Duchoslav, J. L. Campbell, *J. Lipid Res.* **2014**, *55*, 1668–1677.

Acknowledgments

It was a pleasure and privilege to work at the *Fritz Haber Institute* among highly motivated and inspiring people in a well-equipped experimental environment. I thank Prof. Kevin Pagel for giving me the opportunity to work at this exceptional place on an experiment that is so far unique in the world, and for confiding two exciting research projects to me. At this point, I also thank Prof. Gert von Helden, who planned and accompanied the assembly of the Helium Droplet machine and has conducted experiments from the first measurements until today. Further, I would like to thank Prof. Christoph Schalley not only for his willingness to examine this master thesis, but also for his helpful answers and support during five years of being my first contact person of the *Studienstiftung des deutschen Volkes* – which I thank very much for funding. I am also very grateful for the support I got from all the members of the Pagel and von Helden group, in particular from my direct supervisor Eike Mucha. He helped me whenever the experiments were not working for some reason, proof-read the manuscript of this thesis and always had an open ear for me even though he was often submerged by his own work. For proofreading and helpful comments, I also thank Thorren Gimm, Kim Greis and Lilian Maas. Further, I thank the rest of the Helium Droplet team, Daniel Thomas and Maike Lettow, for supporting my experiments and answering any questions about the machine. My questions concerning ion mobility measurements were answered by Christian Manz, Márkó Grabarics and Łukasz Polewski. The IR experiments would not have been possible without the engagement of Wieland Schöllkopf and Sandy Gewinner, who tuned and retuned the FEL to get the best possible energy out of it. The experiments would neither have been possible without the great samples prepared by the groups of Prof. Luc Teyton and Prof. Christoph Arenz, whom I thank all together. Last but not least, I warmly thank my friends, family and office mates for their non-scientific support.

Statutory Declaration

by Carla Kirschbaum, born April 17, 1997 in Berlin

I hereby assert that I have written this master thesis entitled *Gas Phase Infrared Spectroscopy of Glycolipids* entirely by myself using no other resources than those I have indicated. This thesis has not been part of another examination process and has not been published before.

Berlin, August 22, 2019

CARLA KIRSCHBAUM